The Atacama Cosmology Telescope: DR6 Gravitational Lensing Map and Cosmological Parameters

Mathew S. Madhavacheril[1,2], Frank J. Qu[3], Blake D. Sherwin[3,4], Niall MacCrann[3], Yaqiong Li[5], Irene Abril-Cabezas[3], Peter A. R. Ade[6], Simone Aiola[7,8], Tommy Alford[9], Mandana Amiri[10], Stefania Amodeo[11], Rui An[12], Zachary Atkins[8], Jason E. Austermann[13], Nicholas Battaglia[14], Elia Stefano Battistelli[15], James A. Beall[13], Rachel Bean[14], Benjamin Beringue[6], Tanay Bhandarkar[1], Emily Biermann[16], Boris Bolliet[3], J Richard Bond[17], Hongbo Cai[16], Erminia Calabrese[6], Victoria Calafut[17], Valentina Capalbo[15], Felipe Carrero[18], Anthony Challinor[3,4,19], Grace E. Chesmore[9], Hsiao-mei Cho[13,20], Steve K. Choi[5,14], Susan E. Clark[21,22], Rodrigo Córdova Rosado[23], Nicholas F. Cothard[24], Kevin Coughlin[9], William Coulton[7], Kevin T. Crowley[25], Roohi Dalal[23], Omar Darwish[26], Mark J. Devlin[1], Simon Dicker[1], Peter Doze[27], Cody J. Duell[5], Shannon M. Duff[13], Adriaan J. Duivenvoorden[7,8], Jo Dunkley[8,23], Rolando Dünner[18], Valentina Fanfani[28], Max Fankhanel[29], Gerrit Farren[3], Simone Ferraro[25,30], Rodrigo Freundt[14], Brittany Fuzia[31], Patricio A. Gallardo[9], Xavier Garrido[32], Jahmour Givans[23], Vera Gluscevic[12], Joseph E. Golec[9], Yilun Guan[33], Kirsten R. Hall[34], Mark Halpern[10], Dongwon Han[3], Ian Harrison[6], Matthew Hasselfield[7], Erin Healy[8,9], Shawn Henderson[20], Brandon Hensley[23], Carlos Hervías-Caimapo[18], J. Colin Hill[7,35], Gene C. Hilton[13], Matt Hilton[36,37], Adam D. Hincks[38], Renée Hložek[33,38], Shuay-Pwu Patty Ho[8], Zachary B. Huber[5], Johannes Hubmayr[13], Kevin M. Huffenberger[31], John P. Hughes[27], Kent Irwin[21], Giovanni Isopi[15], Hidde T. Jense[6], Ben Keller[5], Joshua Kim[1], Kenda Knowles[37], Brian J. Koopman[39], Arthur Kosowsky[16], Darby Kramer[40], Aleksandra Kusiak[35], Adrien La Posta[32], Alex Lague[1], Victoria Lakey[41], Eunseong Lee[14], Zack Li[17], Michele Limon[1], Martine Lokken[17,33,38], Thibaut Louis[32], Marius Lungu[9], Amanda MacInnis[42], Diego Maldonado[29], Felipe Maldonado[31], Maya Mallaby-Kay[43], Gabriela A. Marques[44], Jeff McMahon[9,43,45,46], Yogesh Mehta[40], Felipe Menanteau[47,48], Kavilan Moodley[37], Thomas W. Morris[49], Tony Mroczkowski[50], Sigurd Naess[51], Toshiya Namikawa[3,52], Federico Nati[28], Laura Newburgh[39], Andrina Nicola[23,53], Michael D. Niemack[5,14], Michael R. Nolta[17], John Orlowski-Scherer[1,54], Lyman A. Page[8], Shivam Pandey[35], Bruce Partridge[55], Heather Prince[27], Roberto Puddu[18], Federico Radiconi[15], Naomi Robertson[56], Felipe Rojas[18], Tai Sakuma[8], Maria Salatino[21,22], Emmanuel Schaan[20,22], Benjamin L. Schmitt[1], Neelima Sehgal[42], Shabbir Shaikh[40], Carlos Sierra[9], Jon Sievers[54], Cristóbal Sifón[57], Sara Simon[44], Rita Sonka[8], David N. Spergel[7,23], Suzanne T. Staggs[8], Emilie Storer[8,54], Eric R. Switzer[24], Niklas Tampier[29], Robert Thornton[1,58], Hy Trac[59], Jesse Treu[61], Carole Tucker[6], Joel Ullom[13], Leila R. Vale[13], Alexander Van Engelen[40], Jeff Van Lanen[13], Joshiwa van Marrewijk[50], Cristian Vargas[18], Eve M. Vavagiakis[5], Kasey Wagoner[8,60], Yuhan Wang[8], Lukas Wenzl[14], Edward J. Wollack[24], Zhilei Xu[1], Fernando Zago[54], and Kaiwen Zheng[8]

[1] Department of Physics and Astronomy, University of Pennsylvania, 209 South 33rd Street, Philadelphia, PA 19104, USA; mathm@sas.upenn.edu
[2] Perimeter Institute for Theoretical Physics, Waterloo, ON N2L 2Y5, Canada
[3] DAMTP, Centre for Mathematical Sciences, University of Cambridge, Wilberforce Road, Cambridge CB3 OWA, UK
[4] Kavli Institute for Cosmology Cambridge, Madingley Road, Cambridge CB3 0HA, UK
[5] Department of Physics, Cornell University, Ithaca, NY 14853, USA
[6] School of Physics and Astronomy, Cardiff University, The Parade, Cardiff CF24 3AA, Wales, UK
[7] Center for Computational Astrophysics, Flatiron Institute, 162 5th Avenue, New York, NY 10010, USA
[8] Joseph Henry Laboratories of Physics, Jadwin Hall, Princeton University, Princeton, NJ 08544, USA
[9] Department of Physics, University of Chicago, Chicago, IL 60637, USA
[10] Department of Physics and Astronomy, University of British Columbia, Vancouver, BC V6T 1Z4, Canada
[11] Université de Strasbourg, CNRS, Observatoire astronomique de Strasbourg, UMR 7550, F-67000 Strasbourg, France
[12] University of Southern California. Department of Physics and Astronomy, 825 Bloom Walk ACB 439, Los Angeles, CA 90089-0484, USA
[13] NIST Quantum Sensors Group, 325 Broadway Mailcode 817.03, Boulder, CO 80305, USA
[14] Department of Astronomy, Cornell University, Ithaca, NY 14853, USA
[15] Sapienza University of Rome, Physics Department, Piazzale Aldo Moro 5, I-00185 Rome, Italy
[16] Department of Physics and Astronomy, University of Pittsburgh, Pittsburgh, PA 15260, USA
[17] Canadian Institute for Theoretical Astrophysics, University of Toronto, Toronto, ON M5S 3H8, Canada
[18] Instituto de Astrofísica and Centro de Astro-Ingeniería, Facultad de Física, Pontificia Universidad Católica de Chile, Av. Vicuña Mackenna 4860, 7820436 Macul, Santiago, Chile
[19] Institute of Astronomy, Madingley Road, Cambridge CB3 0HA, UK
[20] SLAC National Accelerator Laboratory 2575 Sand Hill Road, Menlo Park, CA 94025, USA
[21] Department of Physics, Stanford University, Stanford, CA 94305-4085, USA
[22] Kavli Institute for Particle Astrophysics and Cosmology, 382 Via Pueblo Mall, Stanford, CA 94305-4060, USA
[23] Department of Astrophysical Sciences, Peyton Hall, Princeton University, Princeton, NJ 08544 USA
[24] NASA/Goddard Space Flight Center, Greenbelt, MD 20771, USA
[25] Department of Physics, University of California, Berkeley, CA 94720, USA
[26] Université de Genève, Département de Physique Théorique et CAP, 24 quai Ernest-Ansermet, CH-1211 Genève 4, Switzerland
[27] Department of Physics and Astronomy, Rutgers, The State University of New Jersey, Piscataway, NJ 08854-8019 USA
[28] Department of Physics, University of Milano—Bicocca, Piazza della Scienza, I-3-20126, Milano (MI), Italy
[29] Sociedad Radiosky Asesorías de Ingeniería Limitada, Camino a Toconao 145-A, Ayllu de Solor, San Pedro de Atacama, Chile
[30] Physics Division, Lawrence Berkeley National Laboratory, Berkeley, CA 94720, USA
[31] Department of Physics, Florida State University, Tallahassee, FL 32306, USA
[32] Université Paris-Saclay, CNRS/IN2P3, IJCLab, F-91405 Orsay, France
[33] Dunlap Institute for Astronomy and Astrophysics, University of Toronto, 50 St. George Street, Toronto, ON M5S 3H4, Canada
[34] Center for Astrophysics | Harvard & Smithsonian, 60 Garden Street, Cambridge, MA 02138, USA
[35] Department of Physics, Columbia University, New York, NY 10027, USA

[36] Wits Centre for Astrophysics, School of Physics, University of the Witwatersrand, Private Bag 3, 2050, Johannesburg, South Africa
[37] Astrophysics Research Centre, School of Mathematics, Statistics and Computer Science, University of KwaZulu-Natal, Durban 4001, South Africa
[38] David A. Dunlap Department of Astronomy and Astrophysics, University of Toronto, 50 St George Street, Toronto, ON M5S 3H4, Canada
[39] Department of Physics, Yale University, 217 Prospect Street, New Haven, CT 06511, USA
[40] School of Earth and Space Exploration, Arizona State University, Tempe, AZ 85287, USA
[41] Department of Chemistry and Physics, Lincoln University, Lincoln University, PA 19352, USA
[42] Physics and Astronomy Department, Stony Brook University, Stony Brook, NY 11794 USA
[43] Department of Astronomy and Astrophysics, University of Chicago, 5640 South Ellis Avenue, Chicago, IL 60637, USA
[44] Fermi National Accelerator Laboratory, MS209, P.O. Box 500, Batavia, IL 60510, USA
[45] Kavli Institute for Cosmological Physics, University of Chicago, 5640 S. Ellis Avenue, Chicago, IL 60637, USA
[46] Enrico Fermi Institute, University of Chicago, Chicago, IL 60637, USA
[47] National Center for Supercomputing Applications (NCSA), University of Illinois at Urbana-Champaign, 1205 West Clark Street, Urbana, IL 61801, USA
[48] Department of Astronomy, University of Illinois at Urbana-Champaign, West Green Street, Urbana, IL 61801 USA
[49] Brookhaven National Laboratory, Upton, NY 11973, USA
[50] European Southern Observatory, Karl-Schwarzschild-Str. 2, D-85748 Garching, Germany
[51] Institute of Theoretical Astrophysics, University of Oslo, Norway
[52] Kavli IPMU (WPI), UTIAS, The University of Tokyo, Kashiwa 277-8583, Japan
[53] Argelander Institut für Astronomie, Universität Bonn, Auf dem Hügel 71, D-53121 Bonn, Germany
[54] Physics Department, McGill University, Montreal, QC H3A 0G4, Canada
[55] Department of Physics and Astronomy, Haverford College, Haverford, PA 19041, USA
[56] Institute for Astronomy, University of Edinburgh, Royal Observatory, Blackford Hill, Edinburgh EH9 3HJ, UK
[57] Instituto de Física, Pontificia Universidad Católica de Valparaíso, Casilla 4059, Valparaíso, Chile
[58] Department of Physics, West Chester University of Pennsylvania, West Chester, PA 19383, USA
[59] McWilliams Center for Cosmology, Carnegie Mellon University, Department of Physics, 5000 Forbes Avenue, Pittsburgh, PA 15213, USA
[60] Department of Physics, NC State University, Raleigh, NC 27695, USA

Abstract

We present cosmological constraints from a gravitational lensing mass map covering 9400 deg² reconstructed from measurements of the cosmic microwave background (CMB) made by the Atacama Cosmology Telescope (ACT) from 2017 to 2021. In combination with measurements of baryon acoustic oscillations and big bang nucleosynthesis, we obtain the clustering amplitude $\sigma_8 = 0.819 \pm 0.015$ at 1.8% precision, $S_8 \equiv \sigma_8(\Omega_m/0.3)^{0.5} = 0.840 \pm 0.028$, and the Hubble constant $H_0 = (68.3 \pm 1.1)\,\mathrm{km\,s^{-1}\,Mpc^{-1}}$ at 1.6% precision. A joint constraint with Planck CMB lensing yields $\sigma_8 = 0.812 \pm 0.013$, $S_8 \equiv \sigma_8(\Omega_m/0.3)^{0.5} = 0.831 \pm 0.023$, and $H_0 = (68.1 \pm 1.0)\,\mathrm{km\,s^{-1}\,Mpc^{-1}}$. These measurements agree with ΛCDM extrapolations from the CMB anisotropies measured by Planck. We revisit constraints from the KiDS, DES, and HSC galaxy surveys with a uniform set of assumptions and find that S_8 from all three are lower than that from ACT+Planck lensing by levels ranging from 1.7σ to 2.1σ. This motivates further measurements and comparison, not just between the CMB anisotropies and galaxy lensing but also between CMB lensing probing $z \sim 0.5$–5 on mostly linear scales and galaxy lensing at $z \sim 0.5$ on smaller scales. We combine with CMB anisotropies to constrain extensions of ΛCDM, limiting neutrino masses to $\sum m_\nu < 0.13\,\mathrm{eV}$ (95% c.l.), for example. We describe the mass map and related data products that will enable a wide array of cross-correlation science. Our results provide independent confirmation that the universe is spatially flat, conforms with general relativity, and is described remarkably well by the ΛCDM model, while paving a promising path for neutrino physics with lensing from upcoming ground-based CMB surveys.

Unified Astronomy Thesaurus concepts: Cosmology (343); Observational cosmology (1146); Cosmic microwave background radiation (322); Large-scale structure of the universe (902); Cosmological neutrinos (338); Particle astrophysics (96)

1. Introduction

The cosmic microwave background (CMB) provides a view of the early universe ($z \gtrsim 1100$ or age $t \lesssim 375{,}000$ yr) through primary anisotropies in the relic radiation left over from the hot big bang. Later, as the universe became transparent after recombination, expanded, and cooled, CMB photons continued to experience occasional interactions with structures forming over cosmic time under the influence of gravity. These interactions left behind secondary imprints in the CMB, providing a window into the late-time universe: a view of large-scale structure (LSS) complementary to galaxy and intensity-mapping surveys. In particular, CMB photons travel through all the mass in the observable universe as it develops into LSSs; the ensuing gravitational deflections manifest as distortions on arcminute scales in the CMB that retain coherence over degree scales, the latter corresponding to the size of typical lenses projected along the line of sight ($\sim$300 Mpc). The lensing distortions are distinguished from the Gaussian and statistically isotropic fluctuations in the CMB through the use of quadratic estimators (Hu & Okamoto 2002), resulting in comprehensive mass maps, dominated by dark matter, and probing primarily linear scales. (See Lewis & Challinor 2006 for a review.)

Precise measurements of the CMB on small scales have already allowed the extraction of this secondary lensing signal (probing the late-time universe) from underneath the primary CMB information (probing the early universe). CMB lensing

---

measurements to date include those from the Wilkinson Microwave Anisotropy Probe (WMAP) satellite (Smith et al. 2007); from ground-based surveys such as the Atacama Cosmology Telescope (ACT; Das et al. 2011; Sherwin et al. 2017), the South Pole Telescope (SPT; e.g., van Engelen et al. 2012; Bianchini et al. 2020; Millea et al. 2021), BICEP2/Keck Array (BICEP2 Collaboration et al. 2016), and POLARBEAR (Ade et al. 2014; Faúndez et al. 2020); and from the Planck satellite (Planck Collaboration et al. 2014, 2016c, 2020d; Carron et al. 2022).

While a standard cosmological model has emerged based on precise measurements of the primary CMB anisotropy over the past few decades, it is currently undergoing a stress test. The WMAP measurements of the primary CMB first established that the Lambda cold dark matter (ΛCDM) model with just six parameters is an excellent fit to CMB measurements of the radiation anisotropies of the universe (Spergel et al. 2003; Hinshaw et al. 2013). Measurements from Planck have reinforced this model (Planck Collaboration et al. 2020a). Distinct probes of the geometry, expansion, and growth of structure from a wide range of cosmic epochs have now reached percent-level precision. Many are consistent with the ΛCDM model derived from the primary CMB anisotropy in the early universe (e.g., Freedman et al. 2019; Hamana et al. 2020; Alam et al. 2021; D'Amico et al. 2022; Doux et al. 2022; Aricò et al. 2023; Yu et al. 2023), but some are in tension, with varying levels of significance. A local measurement of the expansion rate, calibrated using Cepheid variable stars, is 7% higher than the prediction from Planck assuming the ΛCDM model (Riess et al. 2022), at quoted 5σ significance. Many measurements of structure growth are $\simeq$10% lower than what the standard model based on Planck parameters predicts (Leauthaud et al. 2017; Hikage et al. 2019; García-García et al. 2021; Hang et al. 2021; Heymans et al. 2021; Abbott et al. 2022; Gatti et al. 2022; White et al. 2022; Chang et al. 2023), at 23σ significance. At the same time, increasingly precise measurements of late-universe observables are quickly opening up a path toward constraining extensions of the standard model, including the mass of neutrinos and the equation of state for the dark energy component purported to cause cosmic acceleration. Ground-based CMB surveys like ACT and SPT, with their high angular resolution, are uniquely positioned to weigh in on these issues from multiple fronts, expanding on the Planck legacy.

In this work, we use ACT Data Release 6 (DR6) to measure gravitational lensing of the CMB and produce a mass map covering 9400 deg². We combine the power spectrum of the fluctuations in this map with measurements of the baryon acoustic oscillations (BAO) measured by 6dF (Beutler et al. 2011) and the Sloan Digital Sky Survey (SDSS; Strauss et al. 2002; Eisenstein et al. 2011; Dawson et al. 2013) to obtain one of the most precise measurements to date of the amplitude of matter fluctuations. Our combination of ACT and Planck lensing along with BAO, in particular, provides a state-of-the art view of structure formation. The first question we ask is whether the amplitude of matter fluctuations is lower than the early-universe prediction from Planck and whether it is in agreement with other late-time measurements (such as optical weak lensing), which probe lower redshifts than CMB lensing does. Here we use our new CMB lensing data to measure the mass fluctuations, primarily from linear scales, dominated by the structures at redshifts $z = 0.5$–5. We also present a suite of constraints on several extensions to the standard cosmological model, including

the sum of masses of neutrinos and deviations of the spatial curvature of the universe from flatness.

This paper is part of a larger set of papers on ACT DR6. It presents our CMB lensing mass map and explores the consequences for cosmology from the combination and comparison of our lensing measurements with other external data (including those in the context of extensions to the ΛCDM model). In Qu et al. (2024), we present the measurement of the CMB lensing power spectrum used in the cosmological constraints of this work, with details on the data analysis and verification pipeline. Qu et al. (2024) also present constraints on cosmological parameters from ACT CMB lensing alone, such as $S_8^{\mathrm{CMBL}} \equiv \sigma_8(\Omega_m/0.3)^{0.25}$. MacCrann et al. (2024) provide a detailed investigation of the characterization and mitigation of our most significant systematic in the lensing power spectrum measurement: the bias due to extragalactic astrophysical foregrounds.

2. A Wide-area High-fidelity Mass Map

High-resolution measurements of the CMB allow us to reconstruct a map of CMB gravitational lensing convergence; this provides a view of the mass distorting the CMB (emitted from the last scattering surface) owing to its gravitational influence. The convergence directly probes the total mass density of the universe integrated along the line of sight all the way to the redshift of recombination $z_\star \simeq 1100$, although nearly all of the contribution comes from redshifts $z < 30$, with peak contributions around $z = 0.5$–5. The convergence is related to the underlying total matter overdensity $\delta_m(\mathbf{x}) = (\rho_m(\mathbf{x}) - \bar{\rho}_m)/\bar{\rho}_m$ (where $\rho_m(\mathbf{x})$ is the matter density and $\bar{\rho}_m$ is the mean matter density) through

$$\kappa(\hat{\mathbf{n}}) = \int_0^\infty dz W^\kappa(z) \delta_m(\chi(z)\hat{\mathbf{n}}, z). \quad (1)$$

In the case of a flat universe with zero spatial curvature, the lensing kernel W^κ simplifies to

$$W^\kappa(z) = \frac{3}{2}\Omega_m H_0^2 \frac{(1+z)}{H(z)} \frac{\chi(z)}{c} \int_z^\infty dz' n(z') \frac{\chi(z') - \chi(z)}{\chi(z')}, \quad (2)$$

where $n(z)$ is the normalized redshift distribution of the light source undergoing gravitational lensing and $\chi(z)$ is the comoving distance to redshift z. While this expression is general (e.g., as appears in cosmic shear distortions of galaxy shapes; see Mandelbaum 2018), when the lensed light source is the CMB, the redshift distribution can be approximated as $n(z) \simeq \delta^D(z - z_\star)$, where $z_\star \simeq 1100$ is the redshift of the surface of last scattering and δ^D is the Dirac delta function. Thus, for the CMB lensing mass maps produced here, we have (Lewis & Challinor 2006)

$$W^{\kappa_{\mathrm{CMB}}}(z) = \frac{3}{2}\Omega_m H_0^2 \frac{(1+z)}{H(z)} \frac{\chi(z)}{c} \left[\frac{\chi(z_\star) - \chi(z)}{\chi(z_\star)} \right]. \quad (3)$$

In Figure 1, we compare the lensing weight kernels for CMB lensing and an illustrative sample of galaxies at $z = 1$, a typical source redshift for current galaxy lensing surveys. CMB lensing provides a complementary view of epochs of the late-time universe that are otherwise difficult to access with galaxy surveys while also significantly overlapping with low-redshift surveys, allowing for a rich variety of cross-correlation analyses.
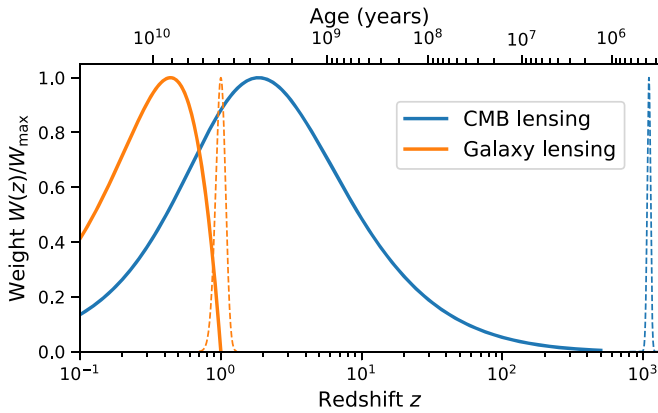
Figure 1. Mass map weights for CMB and galaxy weak lensing, normalized to the maximum value. The blue solid curve shows the relative weights different redshifts receive in a mass map reconstructed from CMB lensing (as in this work), and the orange solid curve shows the same for a sample of galaxies at $z = 1$ (typical of current galaxy lensing surveys). The dashed curves show the corresponding source distribution, with that for the CMB centered at the redshift of last scattering around $z = 1100$. The comoving distances to the peak redshifts are roughly 1 Gpc (galaxy lensing) and 5 Gpc (CMB lensing). An angular scale of ~1° or a lens multipole of $L = 200$ then corresponds to comoving wavenumbers at those distances of roughly 0.2 Mpc^{-1} (galaxy lensing) and 0.04 Mpc^{-1} (CMB lensing).

ACT DR6 Data. The mass map and cosmological parameters in this work are derived from CMB data from ACT. Located on Cerro Toco in the Atacama Desert in northern Chile, ACT observed the sky at millimeter wavelengths from 2007 until 2022. From 2016, the telescope was equipped with the Advanced ACTPol (AdvACT) receiver containing arrays of superconducting transition-edge sensor bolometers, sensitive to both temperature and polarization at frequencies centered roughly at 30, 40, 97, 149, and 225 GHz (Fowler et al. 2007; Thornton et al. 2016); we denote these bands as f030, f040, f090, f150, and f220. Our current analysis uses nighttime temperature and polarization AdvACT data collected from 2017 to 2021 covering the CMB-dominated frequency bands f090 and f150, constituting roughly half of the total volume of data collected by ACT since its inception. Here we use an early science-grade version of the ACT DR6 maps, labeled dr6.01. Since the maps used in our analysis were generated, we have made some refinements to the mapmaking that improve the large-scale transfer function and polarization noise levels, and we include data taken in 2022, although we have performed extensive testing in Qu et al. (2024) to ensure that the dr6.01 map quality is sufficient for lensing analysis. We anticipate using a future version of these maps for further science analyses and for the DR6 public data release. Additionally, data collected during the daytime, at other frequency bands, and during the years 2007–2016 are also not included in the lensing measurement presented here, but we intend to include them in a future analysis.

Software and Pipeline. In order to transform maps of the CMB to maps of the lensing convergence, a preliminary publicly available and open-source pipeline has been developed for the upcoming Simons Observatory (SO; SO Collaboration 2019); we demonstrate this pipeline for the first time on ACT data in this series of papers. The SO stack consists of the pipeline code so-lenspipe,[62] which depends primarily on a reconstruction code falafel,[63] a normalization code tempura,[64] and the map manipulation library pixell.[65] We briefly summarize the measurement here, but the details can be found in our companion paper, Qu et al. (2024).

Producing a Lensing Map. The individual frequency maps are preprocessed and inverse-variance coadded. At f090 and f150, the maps have an average white-noise level of 16 and 17 μK − arcmin, respectively, though there is considerable contribution from correlated atmospheric noise on the largest scales (around 0°.3) used in our analysis, as well as moderate levels of inhomogeneity (see Morris et al. 2022 and Atkins et al. 2023 for details of ACT noise). We use the quadratic estimator formalism (Okamoto & Hu 2003; Planck Collaboration et al. 2020d) to transform maps of the co-added CMB (whose harmonic transform modes we represent with ℓ) to maps of the lensing convergence (whose harmonic transform modes we represent with L); this formalism exploits the fact that gravitational lensing couples previously independent spherical harmonic modes of the unlensed CMB in a well-understood way. We exclude scales in the input CMB maps with multipoles $\ell < 600$ since these contain significant atmospheric noise and Galactic foregrounds. We exclude small scales (multipoles $\ell > 3000$) owing to possible contamination from astrophysical foregrounds like the thermal Sunyaev–Zeldovich (tSZ) effect, the cosmic infrared background (CIB), the kinetic SZ (kSZ) effect, and radio sources. Crucially, we perform "profile hardening" on this estimator (Sailer et al. 2020), a variation of the "bias hardening" procedure (Namikawa et al. 2013; Osborne et al. 2014). This involves constructing a quadratic estimator reconstruction designed to capture mode couplings arising from objects with radial profiles similar to the tSZ imprints of galaxy clusters. We then construct a linear combination of the usual lensing estimator with this profile estimator such that the response to the latter is nulled. The deprojection of contaminants using this profile hardening approach is our baseline method for mitigation of contamination from extragalactic astrophysical foregrounds, though we also obtain consistent results with alternative mitigation schemes, e.g., involving spectral deprojection of foregrounds (Madhavacheril & Hill 2018; Darwish et al. 2021) and shear estimation (Schaan & Ferraro 2019; Qu et al. 2023). The companion paper MacCrann et al. (2024) investigates in detail the bias from foregrounds and shows how our baseline choice fully mitigates the bias from all known sources of foregrounds (including the CIB).

Additionally, our mass maps are made using a novel cross-correlation-based estimator (Madhavacheril et al. 2021): this is a modification of the standard quadratic estimator procedure (Okamoto & Hu 2003) that, through the use of time-interleaved splits, only includes terms that have independent instrument noise. This makes our measurement insensitive to mismodeling of instrument noise.[66] For the released mass map in particular, this ensures that a "mean-field" term we subtract to correct for mask- and noise-induced statistical anisotropy (see, e.g., Benoit-Lévy et al. 2013) does not depend on details of the ACT instrument noise, allowing for the scatter in cross-correlations on large angular scales to be predicted more reliably.

---

[62] https://github.com/simonsobs/so-lenspipe/

[63] https://github.com/simonsobs/falafel/
[64] https://github.com/simonsobs/tempura/
[65] https://github.com/simonsobs/pixell/
[66] This is optimized for current and forthcoming ground-based surveys, which have complicated noise properties owing to the interplay between the atmospheric noise and the telescope scanning strategy.
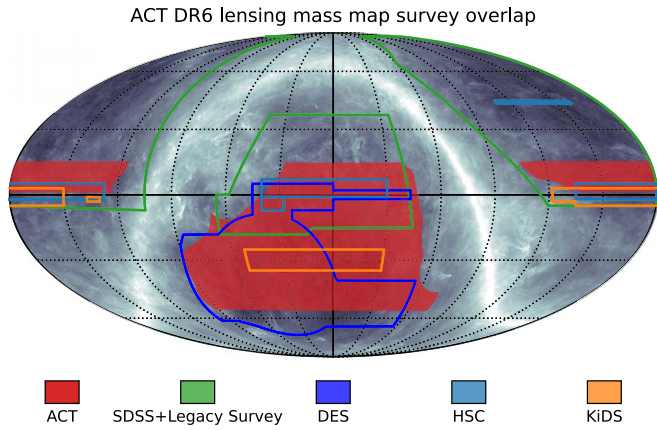
ACT DR6 lensing mass map survey overlap

Figure 2. Overlap of the ACT mass map (red) with various ongoing galaxy surveys. The green contours show a rough union of the footprint of SDSS, the DECam Legacy Survey, and the Mayall z-band Legacy Survey, with DESI data expected to be available in part of this region (Martini et al. 2018; Dey et al. 2019). The grayscale background is a Galactic dust map from Planck (Planck Collaboration et al. 2016a).

While scales with multipoles $600 < \ell < 3000$ are used from the input CMB maps, the output lensing mass maps are made available on larger scales, down to lower multipoles L; this is possible owing to the way large-scale lenses coherently induce distortions in the small-scale CMB fluctuations. For the same reason, most of the information in the lensing reconstruction process comes from small angular scales in the CMB maps with multipoles $\ell > 1500$.

Mass Map Properties. Covering a fraction $f_{\rm sky} \simeq 0.23$ of the full sky, the ACT DR6 CMB lensing mass map overlaps with a number of LSS surveys, providing opportunities for cross-correlations and joint analyses (see Figure 2). In Figure 3, we show a visual representation of the mass map in an orthographic projection, with bright orange corresponding to peaks in the dark-matter-dominated mass distribution and dark purple corresponding to voids in the mass distribution. We also show in Figure 4 a zoom-in of a $900 \deg^2$ region of the mass map in gray scale (bright regions being peaks in the mass and dark regions being voids) overlaid with a map of the CIB constructed by the Planck Collaboration using measurements of the millimeter sky at 545 GHz (Planck Collaboration et al. 2016a). The CIB consists primarily of dusty star-forming galaxies with contributions to the emissivity peaking around $z = 2$ when star formation was highly efficient. Since this also happens to be where the CMB lensing kernel peaks, the CMB lensing maps and the CIB are highly correlated. The high correlation coefficient and the high per-mode signal-to-noise ratio of the ACT mass maps allow us to see by eye the correspondence of the dark-matter-dominated mass reconstruction in gray scale and the CIB density in colored contours.

In Figure 5, we show the power spectra of the reconstruction noise for various mass maps from Planck (which cover 65% of the sky) against the noise power spectrum of the ACT DR6 mass map. The ACT map is signal dominated on scales $L < 150$, similar to the D56 maps from the ACT DR4 release (Darwish et al. 2021), but covering 20 times more area. In comparison to the Planck maps, the ACT mass map has a reconstruction noise power that is at least a factor of two lower, although we note that the Planck maps cover more than twice the area. The small scales are reconstructed with much better precision than Planck, allowing the ACT mass map to be of

particular use in the "halo lensing" regime for cross-correlations with galaxy groups (e.g., Madhavacheril et al. 2015; Raghunathan et al. 2018) and galaxy clusters (e.g., Baxter et al. 2015; Planck Collaboration et al. 2016d; Geach & Peacock 2017; Baxter et al. 2018; Raghunathan et al. 2019; Madhavacheril et al. 2020). There are some associated caveats in this regime that we describe in Section 5.2. Our mass map is also highly complementary to that from galaxy weak lensing with DES (Chang et al. 2018; Jeffrey et al. 2021), which uses source galaxies at redshifts up to $z \simeq 1.5$. This map covers around $4100 \deg^2$ and has significant overlap with the DR6 ACT CMB lensing mass map (see Figure 2).

When using the ACT mass map in cross-correlation, we do not recommend using scales with multipoles $L < 40$, since the null and consistency tests from Qu et al. (2024) suggest that those scales may not be reliable. Similarly, we find evidence in MacCrann et al. (2024) that multipoles $L > 1300$ may not be reliable from the perspective of astrophysical foreground contamination. However, the precise maximum multipole to be used in cross-correlations will be dictated by both theory modeling concerns and improved assessments of foreground contamination specific to the cross-correlation of interest. We enable investigations of the latter by providing a suite of simulated reconstructions that include foregrounds from the Websky extragalactic foreground simulations (Stein et al. 2020).

Lensing Power Spectrum. To obtain cosmological information from the mass map, we compute its power spectrum or two-point function. Since the mass map is constructed through a quadratic estimator and hence has two powers of the CMB maps, the power spectrum is effectively a four-point measurement in the CMB map. This four-point measurement requires subtraction of a number of biases in order to isolate the component due to gravitational lensing. The largest of these biases is the Gaussian disconnected bias, which depends on the two-point power spectrum of the observed CMB maps and is thus nonzero even in the absence of lensing. As discussed in detail in Qu et al. (2024), the use of a cross-correlation-based estimator (Madhavacheril et al. 2021) adds significantly to the robustness of our measurement since the large Gaussian disconnected bias we subtract (see, e.g., Hanson et al. 2011) using simulations does not depend on the details of ACT instrumental noise. This novel estimator also significantly reduces the computational burden in performing null tests (which have no Gaussian disconnected bias from the CMB signal in the standard estimator), since the expensive simulation-based Gaussian bias subtraction can be skipped altogether.

The CMB lensing power spectrum from Qu et al. (2024) is determined at 2.3% precision, corresponding to a measurement signal-to-noise ratio of 43σ. To our knowledge, this measurement is competitive with any other weak-lensing measurement, with precision comparable to that from Planck (Carron et al. 2022) and with complementary information on smaller scales $L > 400$. In Qu et al. (2024), we verify our measurements with an extensive suite of $\mathcal{O}(100)$ map-level and power-spectrum-level null tests and find no evidence of systematic biases in our measurement. These tests include splitting the data by multipole ranges, detector array, frequency band, and inclusion of polarization, as well as variation of regions of the sky masked.

Our analysis followed a blinding policy where no comparisons with previous measurements or theory predictions were allowed until the null tests were passed. Unless otherwise mentioned, the results in this work are based on the "baseline"
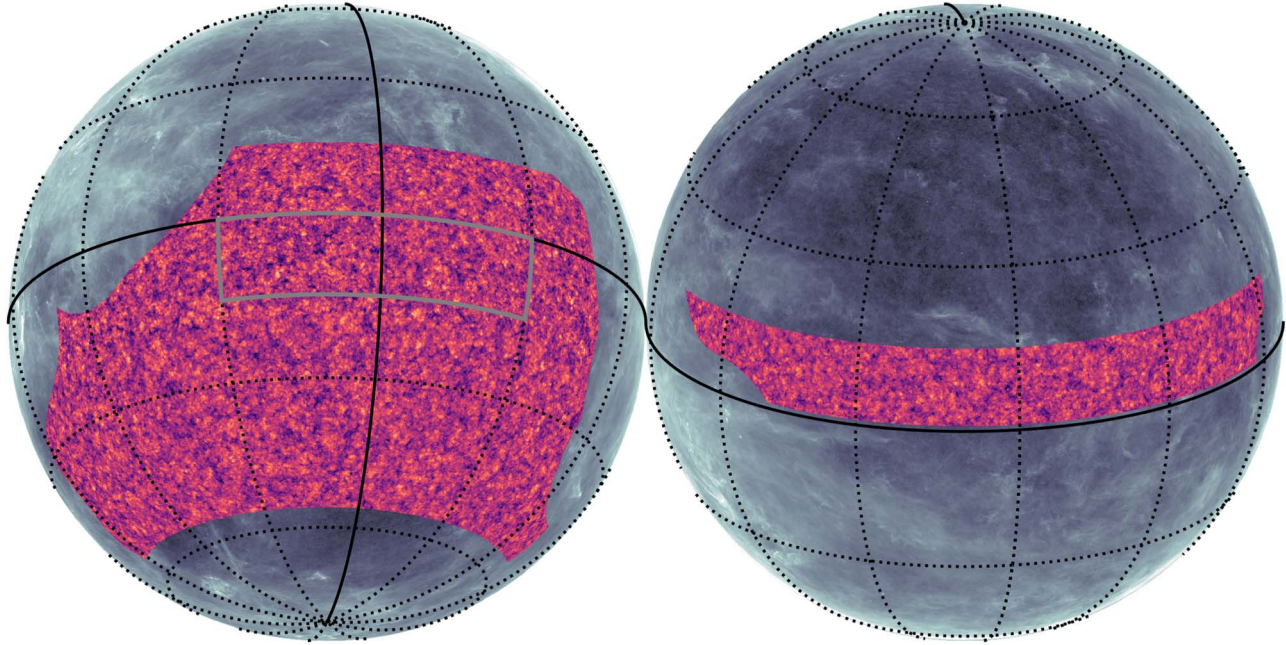
ACT DR6 CMB lensing mass map

Figure 3. ACT DR6 CMB lensing mass map presented in this work. The map covers 9400 deg^2 or sky fraction $f_{sky} = 0.23$ with a signal-to-noise ratio significantly greater than unity over a wide range of scales. We show the Wiener-filtered CMB lensing convergence in an orthographic projection, with bright orange corresponding to peaks of the dark-matter-dominated mass distribution and dark purple regions corresponding to voids. Dark-matter-dominated structures on few-degree scales corresponding to the peak of the lensing power spectrum can be seen by eye (see also Figure 5). The grayscale background is a Galactic dust map from Planck (Planck Collaboration et al. 2016a); our analysis mask is designed to avoid dusty regions of the sky. The region in the gray box is shown in Figure 4.

multipole range of $40 < L < 763$ decided before unblinding. In some cases, we also provide runs with an "extended" multipole range of $40 < L < 1300$, which was deemed to be reliable following a reassessment of foreground biases from simulations (MacCrann et al. 2024) that was done post-unblinding.

3. Is the Amplitude of Matter Fluctuations Low?

We next use the power spectrum of the mass map to characterize the amplitude of matter fluctuations. This allows us to compare our measurement with those from other cosmological probes of structure formation such as galaxy cosmic shear. We focus on the parameter σ_8, which is formally the rms fluctuation in the linear matter overdensity smoothed on scales of 8 Mpc h^{-1} at the present time.[67] Fitting for this parameter therefore requires propagating a model prediction for the linear growth of matter fluctuations over cosmic time to the observed matter power spectrum (projected along the line of sight when using lensing observables).

Different probes of the late universe access different redshifts or cosmic epochs (see Figure 1) and are also sensitive to different scales. Consequently, differences among the inferred values of σ_8 from various late-universe probes or with the early-universe prediction based on CMB anisotropies can hint at possibilities such as (1) nonstandard redshift evolution of the growth of structure, possibly due to modifications of general relativity (e.g., Pogosian et al. 2022; Nguyen et al. 2023); (2) a nonstandard power spectrum of matter fluctuations, e.g., due to axion dark matter (e.g., Rogers et al. 2023) or dark matter–baryon scattering

(e.g., He et al. 2023); (3) incorrect modeling of small-scale fluctuations, e.g., due to nonlinear biasing (for galaxy observables) or baryonic feedback (for lensing observables; e.g., Amon & Efstathiou 2022); or (4) unaccounted-for systematic effects in one or more of these measurements. By providing a measurement of σ_8 with CMB lensing, we probe mainly linear scales with information from a broad range of redshifts $z \sim 0.5$–5, which peaks around $z = 2$ as shown in Figure 1.

We set up a likelihood and inference framework for cosmological parameters detailed in Appendix A, considering a spatially flat ΛCDM universe and freeing up the five cosmological parameters shown in the first section of Table 1: the physical cold dark matter density, $\Omega_c h^2$; the physical baryon density, $\Omega_b h^2$; the amplitude of scalar primordial fluctuations, $\ln(10^{10} A_s)$; the spectral index of scalar primordial fluctuations, n_s; and the approximation to the angular scale of the sound horizon at recombination used in CosmoMC, $100\theta_{MC}$.[68] We note that we have an informative prior on n_s, which is necessary, since the spectral index and the amplitude of fluctuations are degenerate given only a measurement of the lensing power spectrum. As noted in Planck CMB lensing analyses (Planck Collaboration et al. 2016c, 2020d), constraints on the amplitude of fluctuations are only weakly sensitive to the choice of this prior within plausible bounds informed by CMB anisotropies. In particular, this prior is centered on but also five times broader than the constraint obtained from Planck measurements of the CMB anisotropy power spectra in the ΛCDM model (Planck Collaboration et al. 2020c) and two times broader than constraints obtained there from various extensions of ΛCDM. This prior is, therefore, quite conservative. The prior on the baryon density $\Omega_b h^2$ we use is from

---

[67] In our companion paper Qu et al. (2024), we fit for the parameter combination $S_8^{CMBL} = \sigma_8 (\Omega_m/0.3)^{0.25}$; here we isolate σ_8 in order to compare with galaxy weak lensing, which has a different scaling with the matter density Ω_m.
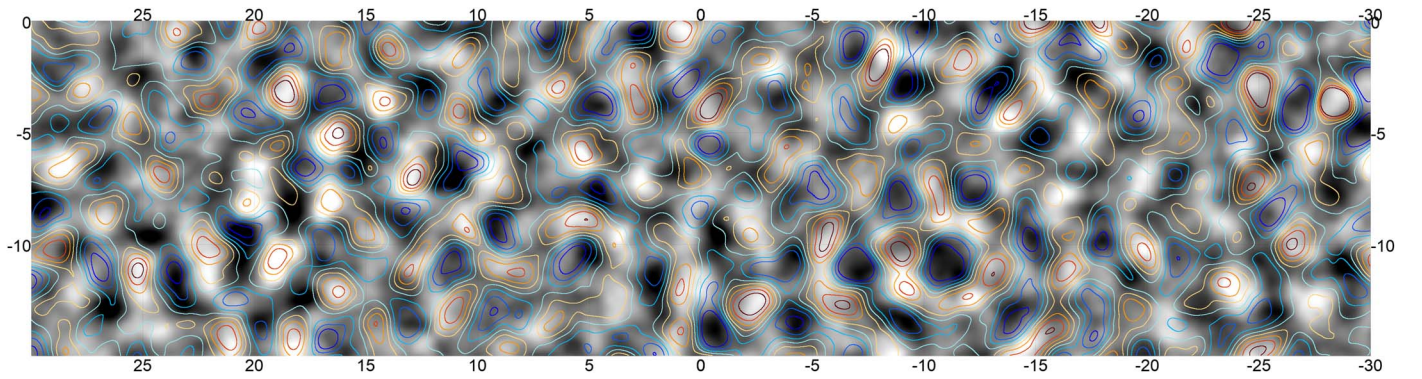
[68] https://cosmologist.info/cosmomc/

Figure 4. A zoom-in of a 900 deg² region of the ACT DR6 mass map shown as the Wiener-filtered gravitational potential (related to the convergence through $\nabla^2\phi = -2\kappa$). The distribution of dusty galaxies constituting the CIB measured by Planck is overlaid as contours. The overdensities in red correspond well with the bright/white mass-dominated regions of the mass map, and the underdensities in blue correspond well with the darker mass-devoid regions.

updated big bang nucleosynthesis (BBN) measurements of deuterium abundance from Mossa et al. (2020), but the constraints are not noticeably degraded using broader priors, e.g., from Cooke et al. (2018).

Importantly, in our comparison here of CMB lensing, galaxy weak lensing, and CMB anisotropies, we fix the sum of neutrino masses $\sum m_\nu$ to be the minimal value of 0.06 eV allowed by neutrino oscillation experiments (with one massive and two massless neutrinos), but we return to constraining this parameter with ACT data in Section 4.2. We also compare our results from CMB lensing with those from the two-point power spectrum of the CMB anisotropies themselves; see Appendix B for details on constraints from the latter that we revisit with our inference framework.

3.1. BAO Likelihoods

Weak-lensing measurements depend primarily on the amplitude of matter fluctuations σ_8, the matter density Ω_m, and the Hubble constant H_0. In order to reduce degeneracies of our σ_8 constraint with the latter parameters and allow for more powerful comparisons of lensing probes with different degeneracy directions, we include information from the 6dF and SDSS surveys. The data we include measure the BAO signature in the clustering of galaxies with samples spanning redshifts up to $z \simeq 1$, including 6dFGS (Beutler et al. 2011), SDSS DR7 Main Galaxy Sample (MGS; Ross et al. 2015), BOSS DR12 luminous red galaxies (LRGs; Alam et al. 2017), and eBOSS DR16 LRGs (Alam et al. 2021). We do not use the higher-redshift emission-line galaxy (Comparat et al. 2016), Lyα (du Mas des Bourboux et al 2020), and quasar samples (Hou et al. 2021), though we hope to include these in future analyses. We only include the BAO information from these surveys (which provides constraints in the Ω_m–H_0 plane) and do not include the structure growth information in the redshift-space distortion (RSD) component of galaxy clustering. We make this choice so as to isolate information on structure formation purely from lensing alone.

3.2. The ACT Lensing Measurement of σ_8

The ACT lensing power spectrum shown in Figure 5 is proportional on large scales to the square of the amplitude of matter fluctuations σ_8 and is therefore an excellent probe of structure growth. This is particularly so in combination with BAO, which does not measure structure growth but whose expansion history information helps break degeneracies with Ω_m

and H_0. In Figure 6 we show constraints in the σ_8–Ω_m plane, and in Figure 7 we show all the sampled parameters. The gray dashed contours from BAO alone do not provide information in the σ_8 direction, and the ACT lensing-alone data set constrains well roughly the parameter combination $\sigma_8(\Omega_m/0.3)^{0.25}$ (see Qu et al. 2024, for further investigation of this combination). The combination of ACT lensing and BAO provides the following 1.8% marginalized constraint (see Table 2):

$$\sigma_8 = 0.819 \pm 0.015. \qquad (4)$$

This is consistent with the value inferred from Planck measurements of the CMB anisotropies that mainly probe the early universe, as can also be seen in the marginalized constraints in Figure 8. Since CMB anisotropy power spectra also contain some information on the late-time universe (primarily through the smoothing of the acoustic peaks due to lensing), we additionally show inferred values of σ_8 where the lensing information has been marginalized over (by freeing the parameter $A_{\rm lens}$; Calabrese et al. 2008)[69] so as to isolate the early-universe prediction from Planck (see Appendix B for more information). Our CMB-lensing-inferred late-time measurement remains consistent with this $A_{\rm lens}$-marginalized prediction of σ_8 from the Planck CMB anisotropies.

Our companion papers Qu et al. (2024) and MacCrann et al. (2024) provide detailed investigations of potential systematic effects in the lensing power spectrum measurement. In Figure 9, we perform inferences of σ_8 in combination with BAO for variations of the mass maps designed to test for our most significant systematic: astrophysical foregrounds. As explained in Qu et al. (2024), while our analysis was carefully blinded, a parallel investigation of the effect of masking and inpainting at the locations of SZ clusters led us to make a change in the pipeline post-unblinding; we find that this resulted in only a 0.03σ shift in σ_8. Similarly, we find consistent results with an alternative foreground mitigation method (CIB deprojection; see MacCrann et al. 2024 for details) and when using polarization data alone, where foreground contamination is expected to be significantly lower,

---

[69] In this paper, as in Calabrese et al. (2008), we use $A_{\rm lens}$ to refer to an amplitude scaling of the lensing that induces smearing of acoustic peaks in the two-point power spectrum while leaving the four-point lensing power spectrum fixed. We caution that the same notation is used in Qu et al. (2024) for a different parameter characterizing the amplitude of the measured four-point lensing power spectrum with respect to a prediction using a ΛCDM cosmology that best fits the Planck CMB anisotropies.
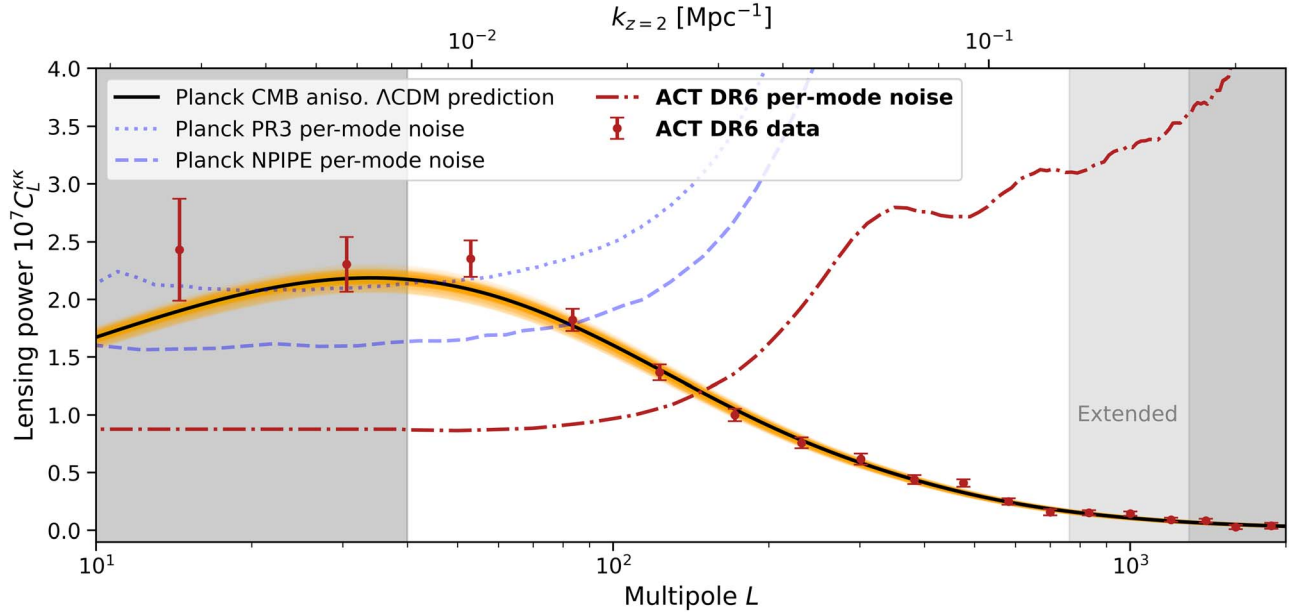
Figure 5. The ACT DR6 CMB lensing power spectrum measurement, from Qu et al. (2024). The band powers of the two-point statistics of the DR6 mass map are shown as red data points. The black solid curve shows the prediction for this signal in the ΛCDM model based on the measurement of the primary CMB anisotropies by the Planck satellite, i.e., this prediction is not a fit to the ACT data. The prediction and our measurement (presented in detail in the companion paper Qu et al. 2024) are in excellent agreement, showing the success of the ΛCDM model in propagating a measurement of the radiation anisotropies at the age of the universe $t \simeq 375{,}000$ yr ($z \simeq 1100$) to the matter fluctuations at $t \simeq 1$–9 billion years ($z \simeq 0.5$–5). We also show samples (orange) from ΛCDM chains of the Planck primary CMB anisotropy measurements to highlight the uncertainty in the early-universe prediction. The dotted, dashed, and dotted–dashed curves show the noise power spectra (i.e., the variance of the reconstruction noise per mode) in the mass maps produced by Planck PR3 (Planck Collaboration et al. 2020d), Planck NPIPE (Carron et al. 2022), and this work, respectively. The ACT mass map is signal dominated out to $L \simeq 150$, providing a high-fidelity view of the dark-matter-dominated mass distribution. The dark-gray regions are not included in our analysis, and the light-gray region is included in our "extended" analyses. The top axis shows the comoving wavenumber $k = L/\chi(z_p)$ at the peak redshift of the CMB lensing kernel $z_p = 2$.

Table 1
Parameters and Priors Used in This Work

Parameter	Prior
Lensing + BAO	
$\Omega_c h^2$	[0.005, 0.99]
$\Omega_b h^2$	$\mathcal{N}(0.02233, 0.00036)$
$\ln(10^{10} A_s)$	[1.61, 4.0]
n_s	$\mathcal{N}(0.96, 0.02)$
$100\theta_{\mathrm{MC}}$	[0.5, 10]
Lensing + BAO + CMB Anisotropies	
$\Omega_c h^2$	[0.005, 0.99]
$\Omega_b h^2$	[0.005, 0.1]
$\ln(10^{10} A_s)$	[1.61, 4.0]
n_s	[0.8, 1.2]
$100\theta_{\mathrm{MC}}$	[0.5, 10]
τ	[0.01, 0.8]
Lensing + BAO + CMB Anisotropies; ΛCDM	
Extensions include the above six and one of below	
$\sum m_\nu$ (eV)	[0.0, 5.0]
Ω_k	[−0.3, 0.3]

Notes. See Section 3 for definitions of the parameters. Uniform priors are shown in square brackets, and Gaussian priors with mean μ and standard deviation σ are shown as $\mathcal{N}(\mu, \sigma)$. In all cases, we additionally reject samples where the derived parameter H_0 falls outside the range [40, 100] km s^{-1} Mpc^{-1}. These prior choices closely follow those in Planck analyses (Planck Collaboration et al. 2016c, 2020d; Carron et al. 2022).

although the uncertainties increase by a factor of two in the latter case. We also test the effect of using linear theory in the likelihood and find a 0.7σ shift, which is expected but not so large as to raise concerns about our dependence on modeling nonlinear scales. In addition, we replace our baseline nonlinear modeling (Mead et al. 2016) with alternative nonlinear model I (Mead et al. 2021 with baryonic feedback) and nonlinear model II (Casarini et al. 2009, 2016) and find negligible shifts. This robustness is expected from results from hydrodynamic simulations (Chung et al. 2020; McCarthy et al. 2021).

3.3. Combination with Planck Lensing

We compare and combine our lensing measurements with those made by the Planck satellite experiment (Planck Collaboration et al. 2020a). We use the NPIPE data release that reprocessed Planck time-ordered data with several improvements (Planck Collaboration et al. 2020e). The NPIPE lensing analysis (Carron et al. 2022) reconstructs lensing with CMB angular scales from $100 \leqslant \ell \leqslant 2048$ using the quadratic estimator. Apart from incorporating around 8% more data compared to the 2018 Planck PR3 release, pipeline improvements were incorporated, including improved filtering of the reconstructed lensing field and of the input CMB fields (by taking into account the cross-correlation between temperature and E-polarization, as well as accounting for noise inhomogeneities; Maniyar et al. 2021). These raise the overall signal-to-noise ratio by around 20% compared to Planck PR3 (Planck Collaboration et al. 2020d). Figure 5 shows a comparison of noise power between the Planck PR3 lensing map and the Planck NPIPE lensing map.[70] The NPIPE mass map covers 65% of the total sky area, compared to the ACT map, which covers 23%, but the ACT map described in Section 2 has a noise power that is at least two times lower, as seen in the same figure.

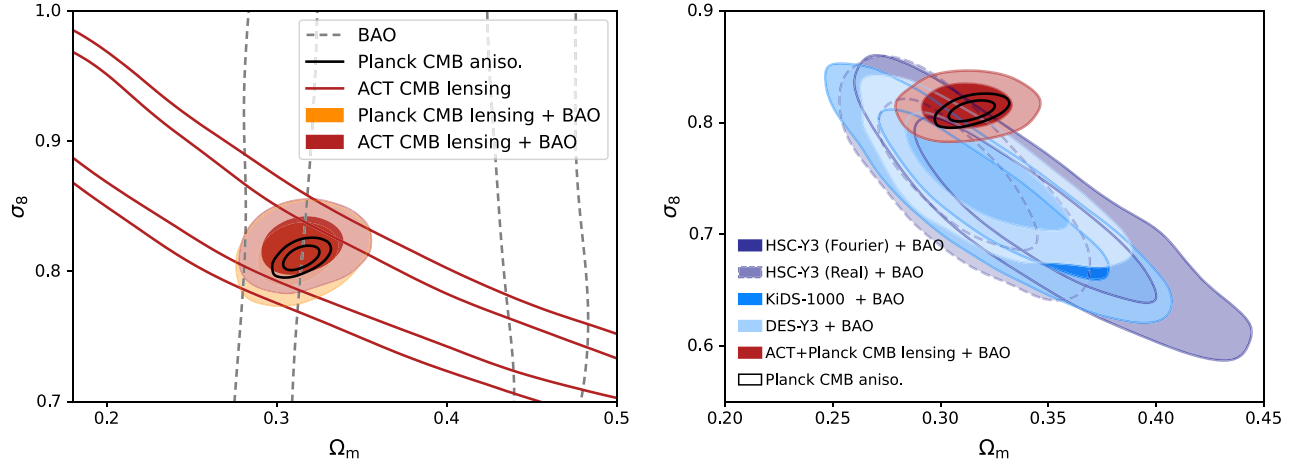[70] The NPIPE noise curve was provided by J. Carron (private communication).

Figure 6. Left: the ACT lensing measurement of the amplitude of matter fluctuations σ_8. For each data set, we show 68% and 95% confidence limits. Lensing measurements also depend on H_0 and Ω_m; we break this degeneracy by including BAO data. The ACT lensing measurement agrees well with the Planck lensing measurement, as well as the inference of σ_8 from Planck CMB anisotropies assuming ΛCDM, a mainly early-universe measurement. Right: comparison of σ_8 measurements between ACT CMB lensing and a consistent reanalysis of galaxy weak-lensing (cosmic shear) data sets. The latter also are degenerate with other parameters (more severely; see Appendix D). All constraints here—except those from Planck CMB anisotropies—include a BBN prior on $\Omega_b h^2$.

Since the `NPIPE` and ACT DR6 measurements only overlap over part of the sky, probe different angular scales, and have different noise and instrument-related systematics, they provide nearly independent lensing measurements. Thus, apart from comparing the two measurements, the consistency in terms of lensing amplitude and the $S_8^{\rm CMBL} \equiv \sigma_8 (\Omega_m/0.3)^{0.25}$ lensing-only constraint as presented in Qu et al. (2024) suggests that we may safely combine the two measurements at the likelihood level to provide tighter constraints. For the `NPIPE` lensing measurements, we use the published `NPIPE` lensing band powers, but we use a modified covariance matrix to account for uncertainty in the normalization in the same way as we do for ACT.[71] We compute the joint covariance between ACT and `NPIPE` band powers using the same set of 480 full-sky FFP10 CMB simulations used by `NPIPE` to obtain the Planck part of the covariance matrix; see Qu et al. (2024) for details. The resulting joint covariance indicates that the correlation coefficient between the amplitudes of the ACT and Planck lensing measurements is approximately 18%. This is expected given the fact that although the ACT and `NPIPE` data sets have substantially independent information, the sky overlap between both surveys means that there is still some degree of correlation between nearby lensing modes.

The combination of ACT lensing, Planck lensing, and BAO provides the following 1.6% marginalized constraint:

$$\sigma_8 = 0.812 \pm 0.013, \qquad (5)$$

which is also consistent with the Planck CMB anisotropy value $\sigma_8 = 0.811 \pm 0.006$ and the WMAP + ACT DR4 CMB anisotropy value $\sigma_8 = 0.819 \pm 0.011$.

3.4. Comparison with Galaxy Surveys

In order to place our constraints in the context of existing measurements, we use the most recently published galaxy weak-lensing measurements from the Dark Energy Survey[72] (henceforth DES-Y3), the Kilo Degree Survey[73] (henceforth

KiDS-1000), and the Hyper Suprime-Cam Subaru Strategic Program[74] (henceforth HSC-Y3). For each survey, we use the weak-lensing shear two-point functions only; we do not include galaxy clustering or cross-correlations between galaxy over-density and shear. While the three surveys provide similar statistical power, each has relative strengths and weaknesses: DES covers the greatest area (approximately 5000 deg^2) with the lowest number density (5.6 galaxies arcmin^{-2}), while HSC-Y3 covers a relatively small area (approximately 416 deg^2) at much higher number density (15 galaxies arcmin^{-2}). KiDS-1000 lies in the middle in both respects and has the advantage of overlap with the VIKING survey (Edge et al. 2013), which provides imaging in five additional near-infrared bands, enabling potential improvements in photometric redshift estimation.

We use the published shear correlation function measurements and covariances from DES-Y3 and KiDS-1000 and Fourier-space and real-space measurements from HSC-Y3. For our DES-Y3 analysis we follow closely Abbott et al. (2022), Amon et al. (2022), and Secco et al. (2022), using the same angular-scale ranges and modeling of intrinsic alignments, while for KiDS-1000 we follow closely Longley et al. (2023), who reanalyzed galaxy weak-lensing data sets, including KiDS-1000 after their initial cosmological analyses in Asgari et al. (2021) and Heymans et al. (2021). We follow the "$\Delta\chi^2$ cut" approach of Longley et al. (2023), removing small-scale measurements to avoid marginalizing over theoretical uncertainty in the matter power spectrum due to baryonic feedback. For HSC-Y3, we show results from the HSC Collaboration, who reran both their Fourier-space and real-space analyses using the parameterization and priors shown in Table 1 in combination with galaxy BAO. We provide further details of our analysis and comparison with published results in Appendix C.

Our results are shown in Figure 8 for two parameter combinations: (1) $S_8 \equiv \sigma_8 (\Omega_m/0.3)^{0.5}$, which is best constrained using galaxy weak lensing; and (2) the amplitude of matter fluctuations σ_8 alone. An interesting aspect of these results is that the σ_8 constraints from CMB lensing combined with BAO are significantly tighter than those from galaxy weak-lensing shear combined with BAO. This difference arises from the different
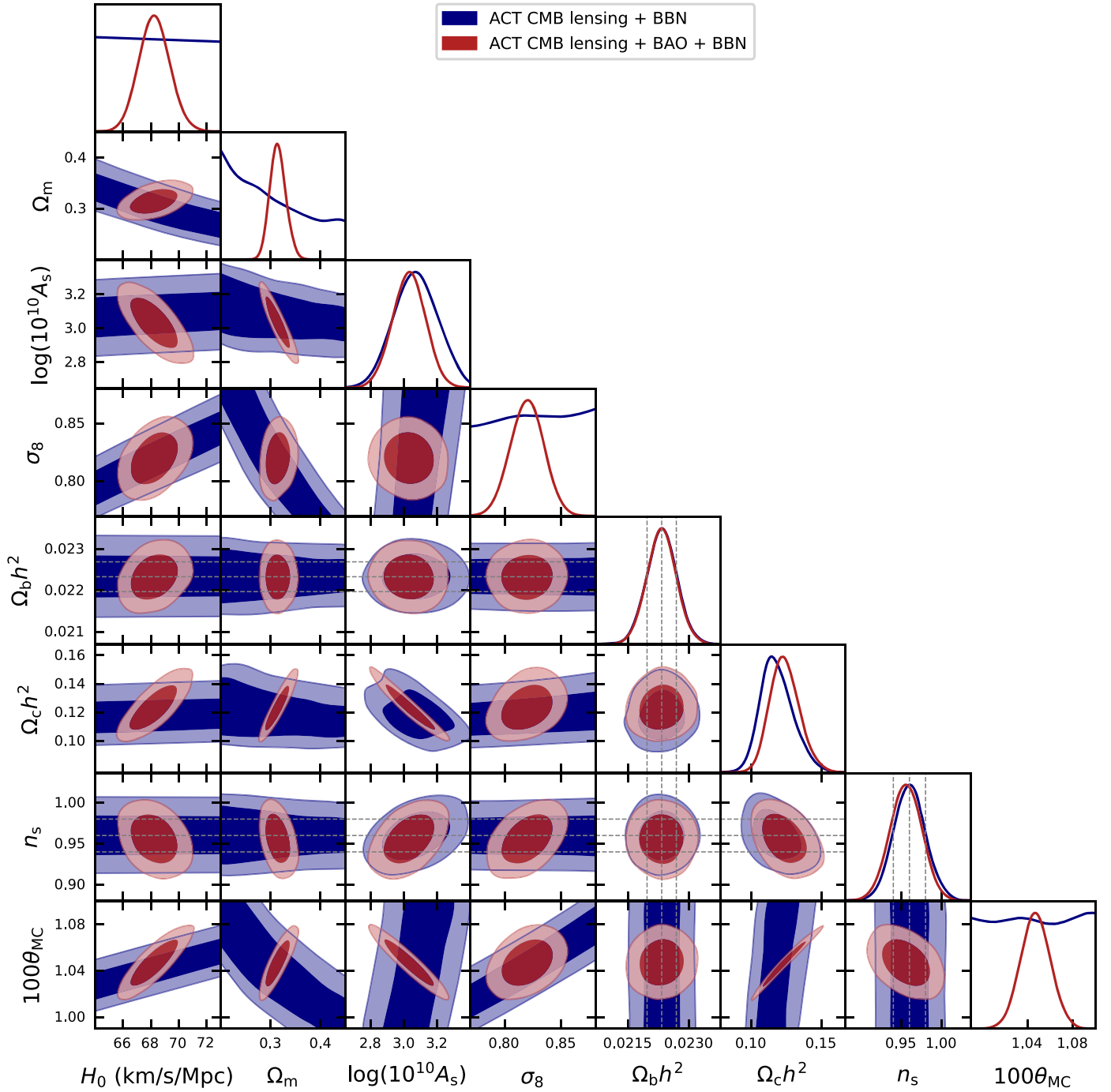

Figure 7. Marginalized 2D and 1D posteriors for ACT CMB lensing either in combination with a BBN prior on $\Omega_b h^2$ (blue; as done in Qu et al. 2024) or in combination with both BBN and galaxy BAO (red). The parameters H_0, Ω_m, and σ_8 are derived, while the remaining are sampled. Informative priors on $\Omega_b h^2$ and n_s are indicated as vertical lines (68% c.l. and mean of priors); all other priors lie well outside the plotted region.

scale dependence of these two lensing observables, with galaxy lensing sensitive to much smaller scales than CMB lensing. We discuss this further in Appendix D.

The CMB lensing measurements from ACT, Planck, and SPTpol (Bianchini et al. 2020)[75] are generally consistent with each other and with the Planck CMB anisotropies. We find that for the S_8 parameter the KiDS measurement, DES

measurement, and HSC measurements (Fourier or real space) are lower than the Planck CMB anisotropy constraint by roughly 2.6σ, 2σ, and 2σ or 2.1σ, respectively. With respect to the ACT+Planck CMB lensing measurement, the KiDS, DES, and HSC measurements are lower by 2.1σ, 1.7σ, and 1.7σ–1.8σ, respectively.

In Figure 10, we show a more comprehensive comparison with a variety of LSS probes. We caution that the probes shown in blue are not reanalyzed with consistent priors but are drawn from the literature. We show constraints in the following categories:

---

[75] The chains for this analysis were provided by the SPT Collaboration; they have a slightly more conservative prior on $\Omega_b h^2$ and do not include eBOSS DR16 LRG BAO, but this should not affect this comparison significantly.

Table 2
Marginalized Constraints on Cosmological Parameters in a Consistent Analysis of Various Weak-lensing Data Sets Shown alongside CMB Anisotropy (Two-point) Constraints

Data	σ_8	S_8	$\Omega_{\rm m}$	H_0 (km s^{-1} Mpc^{-1})
Planck CMB aniso. (PR4 TT+TE+EE) + SRoll2 low-ℓEE	0.811 ± 0.006	0.830 ± 0.014	0.314 ± 0.007	67.3 ± 0.5
Planck CMB aniso. (+$A_{\rm lens}$ marg.)	0.806 ± 0.007	0.817 ± 0.016	0.308 ± 0.008	67.8 ± 0.6
ACT CMB lensing + BAO	0.820 ± 0.015	0.840 ± 0.028	0.315 ± 0.016	68.2 ± 1.1
ACT+Planck lensing + BAO	0.815 ± 0.013	0.830 ± 0.023	0.312 ± 0.014	68.1 ± 1.0
ACT+Planck lensing (extended) + BAO	0.820 ± 0.013	0.841 ± 0.022	0.316 ± 0.013	68.3 ± 1.0
KiDS-1000 galaxy lensing + BAO	0.732 ± 0.049	0.757 ± 0.025	0.323 ± 0.034	68.9 ± 2.0
DES-Y3 galaxy lensing + BAO	0.751 ± 0.035	0.773 ± 0.025	0.319 ± 0.025	68.7 ± 1.5
HSC-Y3 galaxy lensing (Fourier) + BAO	0.719 ± 0.054	0.766 ± 0.029	0.344 ± 0.038	70.2 ± 2.3
HSC-Y3 galaxy lensing (real) + BAO	0.752 ± 0.045	0.760 ± 0.030	0.308 ± 0.024	68.0 ± 1.5

Note. Throughout this work, we report the mean of the marginalized posterior and the 68% confidence limit, unless otherwise mentioned.
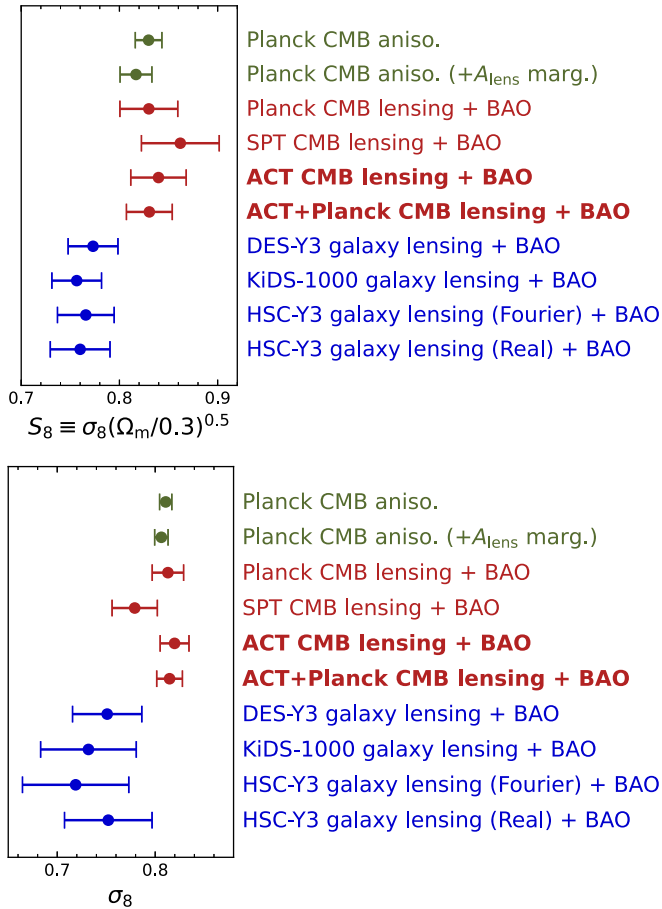
Figure 8. Marginalized posteriors for various combinations of parameters measuring the amplitude of matter fluctuations. The top panel shows $S_8 \equiv \sigma_8(\Omega_{\rm m}/0.3)^{0.5}$, which is best constrained by galaxy lensing, and the bottom panel shows σ_8. All lensing measurements shown here include BAO data. The Planck CMB anisotropy measurements are shown both without and with marginalization over late-time information; while the former is mostly an early-universe extrapolation, the latter is more fully so.

Figure 9. Marginalized posteriors for σ_8 using variations of our ACT lensing analysis in combination with BAO data (black). The SZ inpainting method was our pre-unblinding result (see Qu et al. 2024). We also show variations that use only polarization data and with an alternative CIB deprojection method for mitigating foregrounds. Constraints that use two alternative nonlinear models from Mead et al. (2021; with baryonic feedback) and from Casarini et al. (2009, 2016) are also shown. The constraint that uses linear theory (gray) is not expected to agree perfectly, but the shift is small; together, these show that the details of the nonlinear prescription do not matter significantly.

1. *CMB.* These are CMB (two-point) anisotropy constraints, including our consistent reanalysis of Planck PR4 CMB, with and without marginalization over $A_{\rm lens}$, and WMAP +ACT DR4. This sets our expectation from the mainly primordial CMB view of the early universe.
2. *CMBL.* These are CMB lensing constraints with peak information from around $z = 1$ to 2 from SPTpol (Bianchini et al. 2020), our reanalysis of Planck NPIPE (Carron et al. 2022), our baseline analysis of the new ACT DR6 CMB lensing mass map, and our combination of the latter with Planck NPIPE.
3. *WL.* These are LSS measurements mainly driven by cosmic shear with optical weak lensing, but that may also include galaxy–galaxy lensing and galaxy clustering. We show constraints from the 3×2 pt DES-Y3 cosmology results (Abbott et al. 2022), the KiDS-1000 3×2 pt analysis (Heymans et al. 2021), and the HSC-Y3 galaxy lensing Fourier-space (Dalal et al. 2023) and real-space analyses (Li et al. 2023).
4. *GC.* We show a constraint from galaxy clustering with the BOSS and eBOSS spectroscopic surveys, the final SDSS-IV cosmology analysis with BAO and RSD (Alam et al. 2021),[76] which notably is consistent with CMB aniso-tropies. There have been several independent analyses of BOSS data using effective field theory techniques. While some obtain consistent results (D'Amico et al. 2022; Yu et al. 2023), others (e.g., Philcox & Ivanov 2022; Ivanov et al. 2023) obtain somewhat lower constraints on S_8 despite a large overlap in data.

---

[76] This is obtained from the marginalized statistics of the chains linked here: https://svn.sdss.org/public/data/eboss/DR16cosmo/tags/v1_0_1/mcmc/base/BAORSD_lenspriors/dist/base_BAORSD_lenspriors.margestats
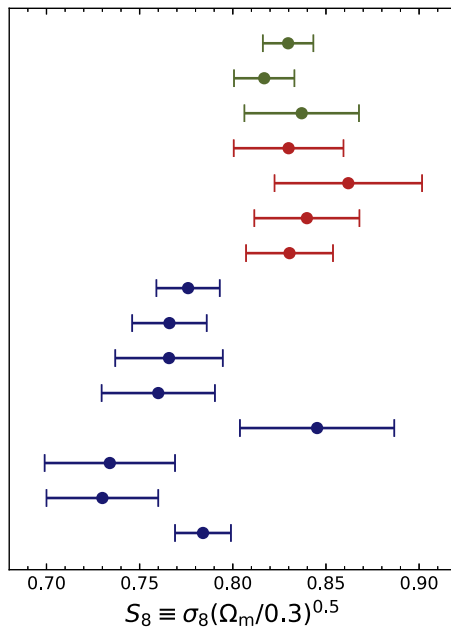
Figure 10. A comparison of $S_8 = \sigma_8(\Omega_m/0.3)^{0.5}$ across multiple probes. We emphasize that the constraints in blue may not be analyzed with consistent choices and priors but are values reported in the literature. Our CMB lensing measurements have relatively higher constraining power for $S_8^{\mathrm{CMBL}} = \sigma_8(\Omega_m/0.3)^{0.25}$ and, in combination with BAO, for σ_8; we refer the reader to Figure 8.

5. *CX.* We show constraints derived from cross-correlations of CMB lensing from SPT and Planck with various galaxy surveys. These include an SPT/Planck CMB lensing cross-correlation with DES galaxies (Chang et al. 2023), a Planck CMB lensing cross-correlation with Dark Energy Spectroscopic Instrument (DESI) LRGs (White et al. 2022), and a Planck CMB lensing cross-correlation with the unWISE galaxy sample (Krolewski et al. 2021). Interestingly, these constraints are lower than those from the Planck CMB anisotropies and our CMB lensing measurement despite also involving CMB lensing mass maps.

We find the general trend of CMB lensing measurements of LSS (probing relatively higher redshifts and more linear scales) agreeing with the early-universe extrapolation from the CMB anisotropies. In contrast, there is a general trend of galaxy weak-lensing probes finding lower inferences of structure growth.

4. Cosmological Constraints on Expansion, Reionization, and ΛCDM Extensions

We now consider other parameters of interest both within ΛCDM and in extended models.

4.1. Hubble Constant

Our DR6 CMB lensing measurements also provide independent constraints on the Hubble constant. The first method by which our lensing results can contribute to expansion rate measurements is via the combination with galaxy BAO data. As seen in Figure 11, if we consider galaxy BAO observations without CMB lensing (but with a BBN prior on the baryon density, which contributes to calibrating the BAO scale via the sound horizon r_d), the constraints on H_0 are still quite weak (open blue contours); this is due to an extended degeneracy direction between H_0 and Ω_m. However, the CMB lensing power spectrum constraints exhibit a degeneracy direction between H_0 and Ω_m that is nearly orthogonal to the BAO constraints. Therefore, the

combination of r_d-calibrated galaxy BAO and CMB lensing allows degeneracies to be broken and tight constraints to be placed on the Hubble constant, as shown in Figures 11 and 12. In particular, from the combination of ACT CMB lensing, galaxy BAO, and a BBN prior, we obtain the constraint

$$H_0 = 68.3 \pm 1.1 \ \mathrm{km \ s^{-1} \ Mpc^{-1}}. \qquad (6)$$

Similarly, using the combination of ACT and Planck CMB lensing together with BAO and a BBN prior, we obtain

$$H_0 = 68.1 \pm 1.0 \ \mathrm{km \ s^{-1} \ Mpc^{-1}}. \qquad (7)$$

Both constraints are consistent with ΛCDM-based Hubble constant inferences from the CMB and LSS and with the tip of the red giant branch (TRGB) calibrated local distance ladder measurements from Freedman et al. (2019) but are in approximately 3.4σ tension with the local distance ladder measurements from SH0ES of $H_0 = 73.04 \pm 1.04 \ \mathrm{km \ s^{-1} \ Mpc^{-1}}$ (Riess et al. 2022).

We expect the above constraints to be primarily derived from the angular and redshift separation subtended by the BAO scale,[77] which is set by the comoving sound horizon at the baryon drag epoch, r_d (Eisenstein & Hu 1998). The majority of current CMB and LSS constraints that are in tension with local measurements from SH0ES derive from this sound horizon scale.[78] This fact has motivated theoretical work to explain the tension by invoking new physics that decreases the physical size of the sound horizon at recombination by approximately 10% (e.g., Aylor et al. 2019; Knox & Millea 2020). This situation motivates new measurements of the Hubble constant that are derived from a different physical scale present in the

---

[77] While we have not proven this, it has been shown that if data sets that calibrate the BAO scale (such as BBN) are included, the BAO feature has the most constraining power and dominates the LSS inference of the Hubble constant (Philcox et al. 2022).

[78] Here we do not make a careful distinction between the sound horizon scale relevant for LSS (r_d) and CMB (r_s) observations, although, to be precise, these are defined at the baryon drag epoch and at photon decoupling, respectively.
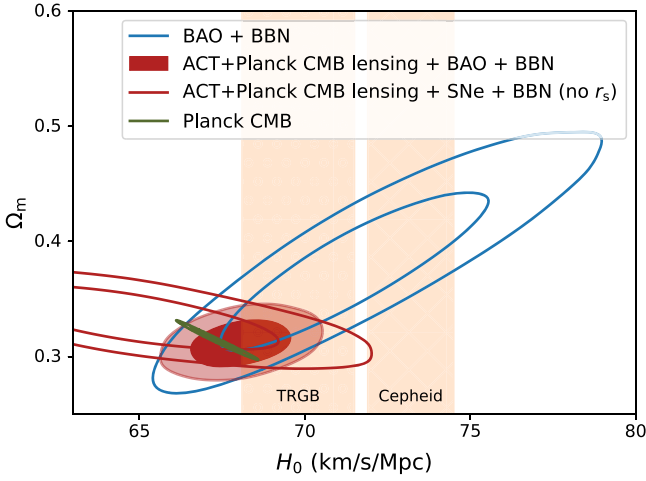
Figure 11. Hubble constant measurements with ACT CMB lensing. The red open contours show a constraint that only utilizes H_0 information from the matter–radiation equality scale in contrast with indirect measurements that typically use the sound horizon scale. The addition of ACT lensing significantly improves the constraint from the combination of galaxy-only BAO and BBN (blue open contours; using the BAO sample discussed in Section 3.1), as can be seen in the red filled contours. The ACT lensing measurements are consistent with the low expansion rate inferred from Planck CMB anisotropies. They are in tension with the Cepheid-calibrated direct inference (Riess et al. 2022) and are consistent with the TRGB-calibrated direct inference (Freedman et al. 2019), whose 68% c.l. bands are shown in orange.
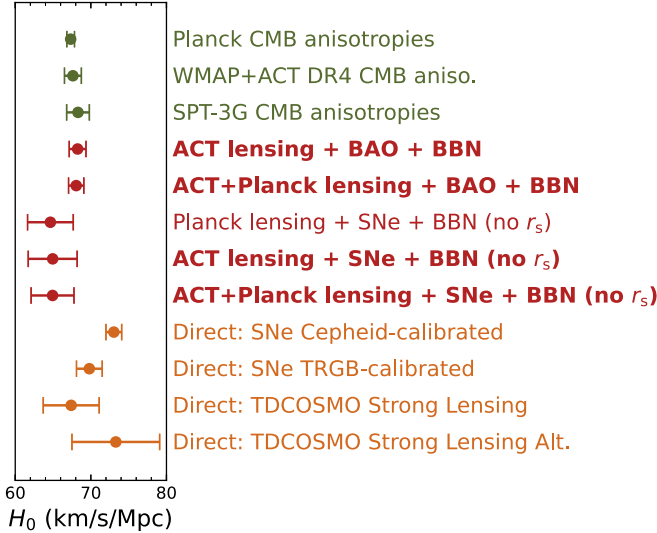
Figure 12. Marginalized posteriors for the Hubble constant from ACT lensing (red). We show constraints both from the combination with BBN and BAO (which depends on the sound horizon r_s) and on a combination with BBN Pantheon+ supernovae (no r_s dependence). We also show various CMB anisotropy measurements that are primarily an early-universe extrapolation (green) and direct inferences of the Hubble constant (orange) from the local universe.

LSS, namely, the matter–radiation equality redshift and scale (with comoving wavenumber k_{eq}), which sets the turnover in the matter power spectrum.

Over the past two years, several measurements of the Hubble constant that rely on the matter–radiation equality information and are independent of the sound horizon scale have been performed, giving results that are consistent with values of H_0 derived from the sound horizon scale (e.g., Baxter & Sherwin 2021; Philcox et al. 2022). Here we repeat the analysis

method used in Baxter & Sherwin (2021) and applied to Planck data to obtain sound-horizon-independent H_0 measurements from both ACT and Planck CMB lensing data and their combination. In particular, we combine CMB lensing power spectra—which are sensitive to the matter–radiation equality scale and, hence, in angular projection, $\Omega_m^{0.6}h$—with uncalibrated supernovae from Pantheon+ (Brout et al. 2022), which independently constrain Ω_m through the shape of the redshift–apparent brightness relation. Here "uncalibrated" refers to the fact that the absolute magnitudes of the supernovae have not been calibrated, e.g., with Cepheid variables or the TRGB technique, such that only information from the relative (not absolute) distance–redshift relation is included. This combination, along with suitable prior choices as in Baxter & Sherwin (2021), allows us to constrain H_0. For the following r_s-independent constraints that exclude BAO, we sample in H_0 instead of $100\theta_{MC}$ and impose a prior of $\Omega_m = 0.334 \pm 0.018$ corresponding to the Pantheon+ (Brout et al. 2022) measurement. With this approach, we obtain from ACT lensing[79]

$$H_0 = 65.0 \pm 3.2 \text{ km s}^{-1} \text{Mpc}^{-1}. \tag{8}$$

With the combination of both Planck and ACT lensing, we have

$$H_0 = 64.9 \pm 2.8 \text{ km s}^{-1} \text{Mpc}^{-1}. \tag{9}$$

As seen in Figure 11, this constraint is also low (at 2.7σ significance) compared to the SH0ES result, although it derives from different early-universe physics than the standard BAO or CMB Hubble constant measurements.

In Figure 12, we show both our marginalized r_s-independent Hubble constant constraints and those from combination with BAO against a compilation of various other indirect and direct constraints. We show in green measurements from the power spectra of the CMB anisotropies, including those described in Appendix B, i.e., from Planck (the combination including NPIPE), from ACT DR4 (the combination with WMAP), as well as the SPT-3G CMB measurement (Dutcher et al. 2021). Among direct measurements, we show the TDCOSMO strong-lensing time-delay measurement with marginalization over lens profiles (Birrer et al. 2020), an alternative TDCOSMO measurement with different lens-mass assumptions (Birrer et al. 2020), the TRGB-calibrated supernova measurement (Freedman et al. 2019), and the Cepheid-calibrated SH0ES supernova measurement (Riess et al. 2022).

The consistency of our r_s-independent and r_s-based inferences of H_0 provides significant support to the idea that the standard ΛCDM model accurately describes the pre-recombination universe. Although r_s-independent H_0 inferences become less constraining in many extended models (Smith et al. 2023), the comparison of r_s-based and r_s-independent constraints is nevertheless a nontrivial null test for ΛCDM (e.g., Farren et al. 2022; Philcox et al. 2022; Brieden et al. 2023), which the model currently passes. The consistency observed here does not provide support to models that attempt to increase the inferred value of H_0 via changes to sound horizon physics.

---

[79] The reader may wonder about the difference—10 km s^{-1} Mpc^{-1} lower here —with the value determined by Baxter & Sherwin (2021), which used Planck + Pantheon. We believe that the change from Pantheon to Pantheon+ is, to a significant extent, responsible for this difference—the Pantheon+ Ω_m is 13% higher than that of Pantheon, which lowers h in this analysis; this also matches what was found in Philcox et al. (2022) using BOSS, Planck lensing, and Pantheon+.

4.2. Neutrino Mass

Observations showing neutrinos oscillating from one flavor to another require these particles to have mass. This is of considerable consequence for particle physics since plausible mechanisms for generating neutrino masses require physics beyond the Standard Model (BSM).[80] Cosmological surveys will provide important constraints in this sector (Allison et al. 2015; Abazajian et al. 2016; DESI Collaboration et al. 2016; SO Collaboration 2019). While neutrino oscillation experiments measure the differences of squared mass $\Delta m_{1,2}^2$ and $|\Delta m_{3,2}^2|$ between pairs of the three mass eigenstates, they do not tell us the absolute scale or sum of the masses. However, given the measured mass-squared differences, we know that the sum of neutrino masses $\sum m_\nu$ must be at least 58 meV for a normal hierarchy (two masses significantly smaller than the third) and 100 meV for an inverted hierarchy (two masses significantly higher than the third). This sets clear targets for experiments that aim to measure the overall mass scale.

Direct experiments like KATRIN (see recent results in Aker et al. 2021) that make observations of tritium beta decay will constrain $\sum m_\nu$ to below 200 meV (90% c.l.) over the next decade.[81] Cosmological observations sensitive to the total matter power spectrum, on the other hand, have already provided stronger constraints (e.g., Planck Collaboration et al. 2020c), albeit contingent on assumptions in the ΛCDM standard model of cosmology. As the universe expands, neutrinos cool and become nonrelativistic at redshifts $z \simeq 200(\sum m_\nu/100 \text{ meV})$. On scales larger than the neutrino free-streaming length, neutrinos cluster and behave like CDM. On smaller scales, their large thermal dispersion suppresses their clustering while their energy density contributes to the expansion rate, also causing the growth of CDM and baryon perturbations to be suppressed. Thus, the net effect is a suppression of the overall (dark-matter-dominated) matter power spectrum on scales smaller than the neutrino free-streaming length.

Cosmological observations do not resolve the scale dependence very well currently, so the dominant signal we look for is an overall suppression of the matter power spectrum relative to that extrapolated from the early-time cosmology measured from the primary CMB anisotropies. Since massive neutrinos suppress the matter power spectrum, and since the CMB lensing power spectrum is a line-of-sight projected integral over this power spectrum, CMB lensing is an excellent probe of massive neutrinos.[82]

We combine our ACT lensing measurement with BAO and CMB anisotropies to obtain constraints on $\sum m_\nu$ in a seven-parameter model (see Table 1).[83] The lensing measurement, together with BAO, provides a handle on the amplitude of matter fluctuations at late times, and the CMB anisotropies
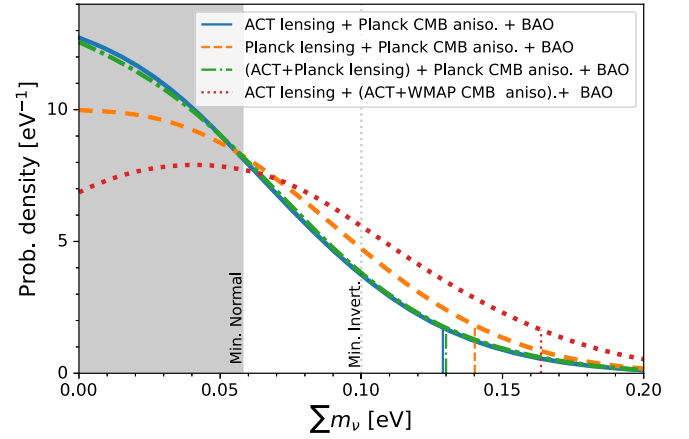
Figure 13. Marginalized posterior probability densities for the sum of neutrino masses from ACT CMB lensing. The vertical lines show the corresponding 95% confidence limits. All constraints here include BAO data, primary CMB anisotropy data, and optical depth information from Planck polarization in addition to CMB lensing. For our baseline constraints, we use CMB anisotropy data from Planck, but we also show with the red dotted curve the constraint obtained when using ACT DR4+WMAP for the CMB anisotropies. With ACT, the posterior is peaked at higher neutrino masses. The minimal sums of masses expected from oscillation experiments in a normal hierarchy and inverted hierarchy are shown as solid gray and dotted gray vertical lines, respectively.

provide an anchor in the early universe that measures primordial fluctuations. The sum of neutrino masses can then be inferred through relative suppression in the matter power at late times; we show our results in Figure 13. Our baseline constraint uses ACT lensing with Planck CMB anisotropies (as well as galaxy BAO and optical depth information from the `SRoll2` reanalysis of the Planck data; see Pagano et al. 2020 and Appendix B):

$$\sum m_\nu < 0.13 \text{eV}; \ 95\% \text{ c.l.} \tag{10}$$

This can be compared to the constraint we obtain when replacing the ACT lensing information with Planck NPIPE lensing of $\sum m_\nu < 0.14$ eV; 95% c. l. . Combining the ACT and Planck lensing measurements, we have

$$\sum m_\nu < 0.13 \text{eV}; \ 95\% \text{ c.l.} \tag{11}$$

The combination of ACT and Planck lensing gives a similar bound to ACT alone despite improving the Fisher information; this is likely due to the lower value of σ_8 preferred by the combination. We also note that analyses that use Planck PR3 CMB anisotropy data, including Planck PR3 lensing (Planck Collaboration et al. 2020d, 2020c) and eBOSS galaxy clustering (Alam et al. 2021), obtain a similar constraint of $\sum m_\nu < 0.12$ eV; 95% c. l. At face value this suggests that adding ACT lensing does not bring new information. However, we note that variations in the Planck CMB anisotropy data have an impact on this upper limit. In particular, Planck PR3 CMB power spectra prefer a high fluctuation in the lensing peak smearing, which tends to lead to a preference for lower neutrino masses and a tighter bound that does not need to be commensurate with the Fisher information in the data set.[84]

---

[80] In some scenarios, measured neutrino masses can map directly onto parameters of BSM Lagrangians like the Majorana phases. See Abe et al. (2023) for recent Majorana neutrino search results from KamLAND-Zen.

[81] The proposed Project 8 could reach a constraint of 40 meV (90% c.l.; Monreal & Formaggio 2009; Ashtari Esfahani et al. 2017, 2021), which would allow for a valuable comparison of a direct measurement with a cosmological measurement even for relatively low mass scales.

[82] This suppression is, however, degenerate with the physical matter density $\Omega_m h^2$, and hence it is crucial to incorporate BAO data that help break this degeneracy (Pan & Knox 2015).

[83] Following the arguments in Lesgourgues & Pastor (2006) and Di Valentino et al. (2018), we consider a degenerate combination of three equally massive neutrinos when varying $\sum m_\nu$.

---

[84] Indeed, the constraint we obtain using Planck PR3 CMB anisotropies is tighter; for the ACT+Planck lensing combination with the extended multipole range, the constraint tightens from $\sum m_\nu < 0.13$ to $\sum m_\nu < 0.12$ eV (95% c. l.) when switching from PR4 to PR3.

This effect is reduced with the Planck PR4 anisotropies (Planck PR4 CMB + BAO alone yields $\sum m_\nu < 0.16$ eV; 95% c.l.) used here, and as a net result, even though we use more data, we recover a similar bound. We also obtain an alternative constraint that swaps the Planck CMB anisotropies with measurements from WMAP and ACT DR4. In this case, the posterior peak shifts to higher values and the bound weakens to

$$\sum m_\nu < 0.16 \text{ eV}; \quad 95\% \text{ c.l.} \tag{12}$$

The constraint on the optical depth to reionization is an important input in these inferences since the suppression of matter power is obtained relative to the measured early-universe fluctuations that are screened (and suppressed) by the reionization epoch (Zaldarriaga 1997). As noted above, our baseline constraints use an updated analysis of low-ℓ Planck polarization data from SRoll2, but we also obtain a constraint on $\sum m_\nu$ using a much more conservative Gaussian prior on the optical depth of $\tau = 0.06 \pm 0.01$:

$$\sum m_\nu < 0.15 \text{ eV}; \quad 95\% \text{ c.l.} \tag{13}$$

4.3. Curvature and Dark Energy Density

Spatial flatness of the universe is a key prediction of the inflationary paradigm underpinning the standard model of cosmology. There has been a suggestion that the Planck CMB anisotropies prefer a closed universe (with curvature parameter $\Omega_k < 0$, where $\Omega_k = 1 - \Omega_m - \Omega_\Lambda$), driven entirely by the moderately high lensing-like peak smearing in Planck measurements of the CMB anisotropies (Di Valentino et al. 2020). It should be noted that this preference for negative curvature density weakens in the recent Planck NPIPE reanalysis of CMB anisotropies (Rosenberg et al. 2022). An independent measurement from ACT DR4+WMAP (Aiola et al. 2020; Choi et al. 2020) is consistent with zero spatial curvature. The combination of BAO and primary CMB data also strongly favors a flat universe.

Nevertheless, we revisit these constraints using CMB data alone. The primary CMB anisotropies alone do not constrain curvature owing to a "geometric degeneracy" (Peebles & Ratra 1988; Efstathiou & Bond 1999) that is broken with the addition of lensing information (Stompor & Efstathiou 1999). Since the ACT and Planck lensing measurements are consistent with the flat ΛCDM prediction, we expect a zero curvature preference to return when including the full lensing information in the mass map, as also seen with Planck data in Planck Collaboration et al. (2020d). We therefore perform inference runs in a ΛCDM+Ω_k extension.

We show our results in Figure 14 in the Ω_Λ–Ω_k plane. The addition of ACT+Planck lensing data to Planck CMB anisotropies gives

$$-0.019 < \Omega_k < 0.002 \quad 95\% \text{ c.l.,} \tag{14}$$

and replacing the CMB anisotropies with those from WMAP +ACT DR4 gives

$$-0.013 < \Omega_k < 0.013 \quad 95\% \text{ c.l.} \tag{15}$$

Both are consistent with spatial flatness. We note that the above constraints only use CMB data and can be equivalently seen as constraining the energy density due to a cosmological constant. For example, as done in Sherwin et al. (2011), we have from CMB data alone, and limiting to ACT lensing alone with
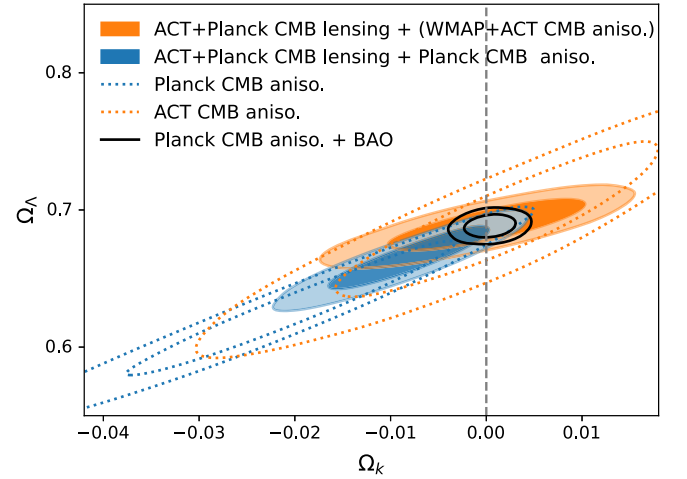
Figure 14. Constraints on spatial curvature and the dark energy density from ACT lensing in a ΛCDM+Ω_k model. The dotted contours show constraints in this plane from CMB anisotropies from ACT DR4 or Planck; these suffer from a geometric degeneracy that is weakly broken with the lensing information in the smearing of the CMB acoustic peaks. Including the full lensing information from our ACT lensing power spectrum significantly reduces this degeneracy and provides (1) consistency with zero spatial curvature and (2) a high-significance detection of a dark energy component from the CMB alone. Addition of BAO data significantly tightens the constraint around zero spatial curvature.

WMAP + ACT DR4 CMB anisotropies,

$$\Omega_\Lambda = 0.68 \pm 0.01 \tag{16}$$

with the accompanying curvature constraint of $-0.016 < \Omega_k < 0.012$ (95% c.l.). While the combination of CMB lensing and CMB anisotropies provides constraints consistent with spatial flatness, we note that combining BAO and CMB anisotropies provides a much tighter constraint. For example, with galaxy BAO and Planck CMB anisotropies, the curvature density is constrained to $-0.003 < \Omega_k < 0.004$ 95% c.l. (see Figure 14). This is not improved significantly with further combination with CMB lensing, but the consistency with flatness from the combination of CMB anisotropy and CMB lensing provides an important cross-check.

4.4. Reionization

In the above analyses, we have used low-ℓ Planck polarization data to break a degeneracy of the late-time matter fluctuation amplitude with the optical depth to reionization τ. This degeneracy arises from the fact that in order to probe effects that change the late-time matter fluctuation amplitude, one must measure and extrapolate from the primordial fluctuations (with amplitude A_s) encoded in the CMB anisotropies. These anisotropies are, however, screened and suppressed during the reionization epoch; the power spectra scale as $A_s^2 e^{-2\tau}$ on intermediate and small angular scales. The low-ℓ CMB polarization "reionization bump" provides the required independent information on the optical depth τ to break this degeneracy.

Measuring polarization at low-ℓ (on large angular scales) is, however, challenging owing to a variety of instrumental and astrophysical systematic effects. It is therefore interesting to turn the question around and ask whether we can infer the optical depth independently from low-ℓ polarization by comparing the CMB-lensing-inferred late-time matter

fluctuation amplitude with the primordial fluctuations in the CMB anisotropies (Planck Collaboration et al. 2016c, 2016b). This requires choosing and fixing a model to perform the extrapolation from the CMB anisotropies to the late-time lensing observations; we choose our baseline ΛCDM model with $\sum m_\nu = 0.06$ eV and the six cosmological parameters varied (see Table 1). Using ACT+Planck lensing, BAO, and Planck CMB anisotropies (excluding low-ℓ polarization), we obtain within this model

$$\tau = 0.074 \pm 0.014, \tag{17}$$

and using WMAP+ACT DR4 CMB anisotropies instead of Planck, we obtain

$$\tau = 0.058 \pm 0.015. \tag{18}$$

These constraints on the optical depth to reionization independent of low-ℓ CMB polarization data are consistent with the value $\tau = 0.059 \pm 0.006$ obtained from the SRoll2 low-ℓ polarization analysis (Pagano et al. 2020).

5. Data Products

This article is accompanied by a release of the likelihood software required to reproduce the ACT cosmological constraints. The CMB lensing mass map will also be made publicly available. In this section, we provide details of these data products.

5.1. Using the Mass Map

The mass map is provided as a FITS file containing the spherical harmonic modes κ_{LM} of the map in a format suitable to be loaded by software like healpy. These can be projected onto desired pixelization schemes, e.g., the HEALPix equal-area pixel scheme, but we note that the map is in an equatorial coordinate system as opposed to the galactic coordinate system of Planck maps. The map has been top hat filtered to remove unreliable scales outside multipoles $40 < L < 3000$; this filter must be forward-modeled in any real-space or stacking analysis. This baseline map is a minimum-variance combination of CMB temperature and polarization information with foreground mitigation through profile hardening, but we also provide variants as described in Section 5.2.

We provide the analysis mask that was used when preparing the input CMB maps. When using the mass map for cross-correlations, it is often necessary to deconvolve the mask, e.g., using the MASTER algorithm (Hivon et al. 2002). We caution that this procedure is not exact in the case of CMB lensing mass maps, since they are quadratic in the input CMB maps. An approximate way to account for this is to use the square of the analysis mask in software packages like NaMaster (Alonso et al. 2019) that implement the MASTER algorithm.

Regardless of the approach used, we strongly encourage users of the mass map to use the provided simulations to test their pipeline for (and estimate) a possible multiplicative transfer function, especially in situations where the area involved in the cross-correlation is significantly smaller than the ACT mass map. We provide both simulated reconstruction maps and the input lensing convergence maps for this purpose.

5.2. Cluster Locations, Astrophysical Foregrounds, and Null Maps

The standard quadratic estimator we have used (Hu & Okamoto 2002) suffers from a known issue at the location of massive clusters; the reconstruction becomes biased low in these regions owing to higher-order effects (Hu et al. 2007). For this reason, we provide a mask of SZ clusters to avoid when stacking. Cross-correlations with most galaxy samples should not be affected.

We also provide lensing reconstructions run on simulations that contain the Websky implementation of extragalactic foregrounds (Stein et al. 2020). We encourage users of the mass maps to implement a halo occupation distribution (HOD) for their galaxy sample of interest into the Websky halo catalog so as to test with these simulations for any possible residual foreground bias. These simulations can also be used to test for possible effects due to correlations between the mask and LSS (see, e.g., Surrao et al. 2023). For similar purposes, we provide a suite of null maps (e.g., lensing reconstruction performed on the difference of 90 and 150 GHz maps) that can be cross-correlated with LSS maps of interest. We additionally provide the following variants of the lensing map that can be used to assess foreground biases: (1) one that utilizes only CMB polarization information, (2) one that utilizes only CMB temperature information, and (3) one that uses an alternative foreground mitigation procedure involving spectral deprojection of the CIB.

5.3. Likelihood Package and Chains

We provide the band powers of the lensing power spectrum measurement, a covariance matrix, and a binning matrix that can be applied to a theory prediction. We also provide a Python package that contains a generic likelihood function, as well as an implementation for the Cobaya Bayesian inference framework. We provide variants corresponding to both the pre-unblinding "baseline" multipole range of $40 < L < 763$ and the "extended" multipole range of $40 < L < 1300$, set after unblinding.

6. Conclusion and Discussion

We have used ACT CMB data from 2017 to 2021 to provide a new view of LSS through gravitational lensing of the CMB, providing a high-fidelity wide-area mass map covering $9400\,\mathrm{deg}^2$ to the community for further cross-correlation science. Through a study of the power spectrum of this mass map, measured in Qu et al. (2024), in combination with BAO data, we find that the amplitude of matter fluctuations σ_8 is consistent (at 1.8% precision) with the expectation from the ΛCDM model fit to measurements of the CMB anisotropies from Planck that probe mainly the early universe. We find that a consistent reanalysis of galaxy weak-lensing (cosmic shear) data with identical prior choices shows all three of DES, HSC, and KiDS to be lower than Planck anisotropies at varying levels ranging from 2σ to 2.6σ and lower than our ACT +Planck lensing measurement at varying levels ranging from 1.7σ to 2.1σ. We find a CMB-lensing-inferred value of the Hubble constant H_0 consistent with Planck ΛCDM and inconsistent with Cepheid-calibrated supernovae; this persists even when analyzing a variant of our measurement that does not derive information from the sound horizon. Our joint ACT +Planck lensing constraint on the sum of neutrino masses

$\sum m_\nu < 0.13$ eV (95% c. l.) and $\sum m_\nu < 0.16$ eV (99% c. l.) provides a robust measurement that relies on mostly linear scales. With CMB data alone, informed by ACT lensing, we find that the universe is consistent with spatial flatness and requires a dark energy component.

We have only considered a subset of interesting model extensions here. Our publicly released likelihoods encapsulate linear scales of the total matter density field primarily over the redshift range $z = 0.5–5$. A variety of follow-up investigations will be of interest, including those that combine with galaxy lensing and clustering covering a range of redshifts and scales, possibly fitting these measurements jointly with models that look for nonstandard dark matter physics and modifications of general relativity. An exciting near-term prospect is an exclusion of the inverted hierarchy of massive neutrinos; for example, improved BAO data from the ongoing DESI (DESI Collaboration et al. 2016) will significantly reduce the degeneracy of our $\sum m_\nu$ measurement with the matter density Ω_m (Allison et al. 2015).

The publicly released mass maps can be used for a variety of cross-correlations; those with galaxy surveys, for example, can produce improved constraints on local primordial non-Gaussianity f_{NL} (Schmittfull & Seljak 2018; McCarthy et al. 2023), as well as constraints on the amplitude of structure as a function of redshift $\sigma_8(z)$ (e.g., White et al. 2022). The mass maps can be combined with measurements of the tSZ and kSZ effects along with X-ray measurements to study the thermodynamics of galaxy formation and evolution by supplementing electron pressure, density, and temperature measurements with gravitational mass on arcminute scales (Battaglia et al. 2017; Bolliet et al. 2023). They can also be used to study the nonlinear universe, providing an unbiased view of the distribution of voids and filaments (e.g., He et al. 2018; Raghunathan et al. 2020).

ACT completed observations in 2022, but several possibilities lie ahead for significantly improved mass maps and cosmological constraints. In particular, we will explore the fidelity of roughly 50% of ACT data collected (mostly during the daytime) that were not used in this analysis. Data at lower frequencies and at 220 GHz can be used to enhance the foreground cleaning, which, in combination with hybrid mitigation strategies (Darwish et al. 2022), may allow us to use higher multipoles in the CMB lensing reconstruction. Other areas of exploration include (1) optimal filtering of ACT maps that accounts for noise nonidealities (Mirmelstein et al. 2019), (2) CMB-map-level combination with Planck data, (3) improved accuracy and precision of the lensing signal at the location of galaxy clusters (Hu et al. 2007), and (4) improved compact-object treatment allowing for less aggressive masking of the galaxy, thus enabling larger sky coverage of the mass map.

Looking further ahead, the Simons Observatory (SO Collaboration 2019), under construction at the same site as ACT, will significantly improve the sensitivity of CMB maps. This will enable subpercent constraints on the amplitude of matter fluctuations and a wide variety of cosmological and astrophysical science goals.

Acknowledgments

Appendix A
Lensing (Four-point) Likelihood and Theory

In this appendix, we describe in more detail the components of our lensing likelihood. We approximate this as being Gaussian in the band powers of the estimated lensing power spectrum $\hat{C}_{L_b}^{\kappa\kappa}$:

$$-2\ln\mathcal{L} = \sum_{bb'}[\hat{C}_{L_b}^{\kappa\kappa} - C_{L_b}^{\kappa\kappa}(\boldsymbol{\theta})]\mathbb{C}_{bb'}^{-1}[\hat{C}_{L_b}^{\kappa\kappa} - C_{L_{b'}}^{\kappa\kappa}(\boldsymbol{\theta})], \quad (A1)$$

where $C_{L_b}^{\kappa\kappa}$ is the theory lensing convergence power spectrum evaluated with cosmological parameters $\boldsymbol{\theta}$ and $\mathbb{C}_{bb'}$ is the baseline covariance matrix for the binned spectrum, obtained from realistic sky simulations and detailed in Qu et al. (2024). When combining the lensing likelihood with that for the CMB anisotropy power spectra, we ignore the covariance between the measured lensing and anisotropy spectra, as these are negligible for DR6 noise sensitivities (Schmittfull et al. 2013; Peloton et al. 2017).

The reconstructed CMB lensing power spectrum depends on the four-point function of the CMB fields and, thus, quadratically on the CMB anisotropy power spectra. We normalize the estimated lensing power spectrum with a fiducial choice of CMB power spectra, but we account for the cosmology dependence of the true normalization (and of one of the bias corrections) in the likelihood analysis. For joint constraints with CMB anisotropy spectra, we correct the normalization at each point in parameter space as discussed below. For cosmology runs that do not include information from the primary CMB, we effectively marginalize over realizations of the CMB power spectrum in the normalization,

informed by current constraints. Specifically, we obtain 1000 posterior samples from the ACT DR4 + Planck primary CMB chains and propagate these to the covariance matrix as described in Appendix B of Qu et al. (2024). This step is done consistently to both the ACT and the NPIPE parts of the covariance matrix.

A fiducial cosmology $\boldsymbol{\theta}_0$ is assumed in various steps of the lensing measurement. This includes the calculation of the normalization $\mathcal{R}_L^{-1}$ and N_L^1 bias. To account for the dependence on $\boldsymbol{\theta}_0$, the theoretical lensing power spectrum at each sampled point $\boldsymbol{\theta}$ needs to be corrected as

$$C_{L_b}^{\kappa\kappa,\text{th}}(\boldsymbol{\theta}) = \frac{[\mathcal{R}_{L_b}^{-1}(\boldsymbol{\theta}_0)]^2}{[\mathcal{R}_{L_b}^{-1}(\boldsymbol{\theta})]^2}C_{L_b}^{\kappa\kappa}(\boldsymbol{\theta}) - N_{L_b}^1(\boldsymbol{\theta}_0) + N_{L_b}^1(\boldsymbol{\theta}). \quad (A2)$$

Fully calculating the above for each point in the sampled parameter space is unfeasible, and hence we follow the approach of Planck Collaboration et al. (2016c), Sherwin et al. (2017), and Planck Collaboration et al. (2020d) and forward-model the linearized corrections to the theory spectrum due to the parameter deviations from the fiducial cosmology. For small deviations, expanding the normalization and $N_{L_b}^1$ around $\boldsymbol{\theta}$ leads to

$$C_{L_b}^{\kappa\kappa,\text{th}}(\boldsymbol{\theta}) \approx C_{L_b}^{\kappa\kappa}(\boldsymbol{\theta}) + 2\frac{d\ln\mathcal{R}_{L_b}(\boldsymbol{\theta}_0)}{dC_{\ell'}^j}$$

$$\times [C_{\ell'}^j(\boldsymbol{\theta}) - C_{\ell'}^j(\boldsymbol{\theta}_0)]C_{L_b}^{\kappa\kappa}(\boldsymbol{\theta}_0) + \frac{dN_{L_b}^1}{dC_{\ell'}^j}[C_{\ell'}^j(\boldsymbol{\theta}) - C_{\ell'}^j(\boldsymbol{\theta}_0)]$$

$$+ \frac{dN_{L_b}^1}{dC_{L_b'}^{\kappa\kappa}}[C_{L_b'}^{\kappa\kappa}(\boldsymbol{\theta}) - C_{L_b'}^{\kappa\kappa}(\boldsymbol{\theta}_0)].$$

$$(A3)$$

The corrections involving changes in the CMB 2-point spectra (second and third terms on the RHS above) are not included for runs that combine with the ACT DR4 CMB 2-point likelihood. This is motivated following Appendix B of Qu et al. (2024) where it is noted that the ACT DR6 maps used in this work are calibrated against *Planck* maps, and the calibration uncertainty in this process is significantly smaller than that for the maps involved in the ACT DR4 2-point CMB cosmology analysis. We have checked that an MCMC run that includes the above terms returns parameter constraints similar to those when the corrections are excluded, if the chain point spectra $C_{\ell'}^j(\boldsymbol{\theta})$ are rescaled through calibration of $C_{\ell'}^{TT}(\boldsymbol{\theta})$ against *Planck* in the multipole range $1000 < \ell < 2000$. This procedure closely approximates what was done for the ACT DR6 data. For theory predictions, we use the Einstein–Boltzmann code CAMB (Lewis et al. 2000; ver. 1.3.6)[85] with sufficiently high accuracy lmax = 4000, lens_margin = 1250, lens_potential_accuracy = 4, Accuracy-Boost = 1, lSampleBoost = 1, and lAccuracy-Boost = 1. While these are lower than recommended in McCarthy et al. (2022)—see Appendix A of Hill et al. (2022) for the importance to current-generation CMB surveys—the evaluation time is significantly lower while being of sufficient accuracy given the precision of our measurement. We use the mead2016 nonlinear matter power spectrum prescription (Mead et al. 2015, 2016) with the default parameters

---

[85] https://camb.info/

`HMCode_A_baryon = 3.13` and `HMCode_eta_baryon = 0.603`. Since our measurement mainly probes linear scales, this choice and baryonic feedback effects do not matter at current sensitivities, which can be explicitly seen in our analysis in Figure 9. For runs that include the ACT DR4 CMB anisotropy likelihood (see Appendix B), power spectra are calculated out to `lmax = 7000`. We have confirmed that χ^2 values from this likelihood only differ by 0.04% when using accuracy settings from McCarthy et al. (2022), and so we do not use higher accuracy settings for ACT DR4.

We perform our Markov Chain Monte Carlo (MCMC) inference using the `Cobaya` package (Torrado & Lewis 2021) with the Metropolis–Hastings (MH) sampler with adaptive covariance learning, and we run our chains until the Gelman–Rubin criterion (Gelman & Rubin 1992) for chain variances falls below $R - 1 = 0.01$, except in cases where the curvature density is varied, where we only require a threshold of $R - 1 = 0.02$.

Appendix B
CMB Anisotropy (Two-point) Likelihoods

While our baseline constraint on structure growth only uses the ACT (and in some cases Planck) gravitational lensing reconstruction measurements in this work, we sometimes use information from the primary CMB anisotropies themselves either for comparison or in combination with the lensing measurement. CMB experiments like Planck and ACT produce maps of the temperature (T) and polarization anisotropies (E-mode and B-mode). The angular power spectra of these maps (TT, TE, EE) provide information mainly on the primary anisotropies of the CMB, which depend on the early universe (redshifts $z > 1100$). They, however, also are screened by reionization ($z \simeq 8$) and therefore have a dependence on the optical depth to that epoch, τ, and pick up secondary anisotropies like lensing. Reionization produces a suppression of the power spectra (as well as enhanced low-ℓ polarization), and the lensing effect induces smearing of the CMB acoustic peaks and a transfer of power from large to small scales. While the anisotropy power spectra measurements still mainly provide an early-universe extrapolation of late-time parameters like σ_8, in some cases we marginalize over an A_{lens} parameter that frees up the amplitude of the lensing-induced peak smearing. This isolates the early-universe information so as to allow comparison with the late-time CMB lensing reconstruction (through the CMB four-point function) and with galaxy lensing.

As our baseline for CMB anisotropies, we use data measuring the two-point function from Planck. For the low-ℓ temperature component, we use the likelihood at $\ell < 30$ derived from the PR3 maps (Planck Collaboration et al. 2020b). For the high-ℓ temperature and polarization, we use the likelihood for TT, TE, and EE presented in Rosenberg et al. (2022), derived from the `NPIPE` maps (Planck Collaboration et al. 2020e) using the `CamSpec` likelihood. This gives consistent results to PR3 (Planck Collaboration et al. 2020b; Efstathiou & Gratton 2021), with around 10% more constraining power.

To include information from Planck's large-scale polarization data that constrains the optical depth to reionization, we use the likelihood estimated in Pagano et al. (2020) from the `Sroll2` maps, sampling from the `Sroll` likelihood released with PR3 but updating the data with `Sroll2`.[86]

We also form a second independent combination of two-point function data by combining the WMAP 9 yr likelihood with the ACT DR4 likelihood, for TT, TE, and EE. For WMAP we use the Python implementation of the $\ell > 23$ likelihood, `pyWMAP`.[87] For ACT we use the DR4 foreground-marginalized `pyactlite` likelihood software.[88] In this case, we discard the large-scale WMAP polarization data, keeping the information on the optical depth from the Planck `Sroll2` likelihood. In some cases we also test the effect of using the Planck PR3 high-ℓ likelihood in place of the `NPIPE` likelihood and of approximating the optical depth with a Gaussian distribution with mean and error shifted compared to the `Sroll2` measurement.

Appendix C
Reanalysis of Galaxy Weak Lensing

We perform our galaxy weak-lensing analysis (cosmic shear) parameter inference using the `CosmoSIS` (Zuntz et al. 2015) framework. To facilitate a consistent comparison, the reanalysis here departs from the published works from KiDS and DES in the following ways: (1) we choose the cosmological parameterization from Table 1 (i.e., we sample in $\ln(10^{10}A_s)$, $100\theta_{\text{MC}}$, $\Omega_c h^2$, $\Omega_b h^2$ instead of A_s, Ω_c, Ω_b, H_0); (2) we choose the priors from Table 1, most notably a broader prior on H_0 and a sharper prior on n_s; (3) we have minor differences in the version and accuracy of the CAMB Boltzmann code (see Appendix A); and (4) we sample using the MH sampler instead of a nested sampler. These choices match those from Planck analyses (Planck Collaboration et al. 2016c, 2020d). For the MH sampling, we use adaptive covariance learning through an interface with the `Cobaya` package (Torrado & Lewis 2021) and run our chains until the Gelman–Rubin criterion (Gelman & Rubin 1992) for chain variances falls below $R - 1 = 0.05$. We use the `tensiometer` package[89] (Raveri et al. 2020; Raveri & Doux 2021) to load `CosmoSIS` outputs into `getdist` (Lewis 2019); the latter is used throughout this work to obtain marginalized 1D and 2D densities from MCMC samples. All reported tensions in this work use a Gaussian metric, i.e., the difference in the mean of the marginalized posteriors divided by the quadrature sum of the 68% confidence limits for the parameter of interest. The HSC reanalyses shown here were provided by the HSC team. They were run with the same priors and parameterization as above, with the same combination of galaxy BAO, but differ in the Boltzmann codes and sampling techniques.

In Figure 15, we compare the constraints from the reanalysis (blue) with those in the literature (orange). The "galaxy lensing" constraints all only include cosmic shear measurements, whereas "$3 \times 2\,\text{pt}$" measurements also include galaxy clustering and galaxy–galaxy lensing. Our DES-Y3 reanalysis constraints on $\sigma_8(\Omega_m/0.3)^{0.5}$ that include BAO are in agreement with those from the DES-Y3 galaxy-lensing-alone analysis in Amon et al. (2022) and Secco et al. (2022), the Fourier variant of the former (Doux et al. 2022), and the DES-Y3 $3 \times 2\,\text{pt}$ analysis in Abbott et al. (2022). Similarly, our KiDS-1000 reanalysis constraints that include BAO are in agreement with those from the galaxy lensing reanalysis in Longley et al. (2023; whose framework we follow, including for scale cuts),

---

[86] https://web.fe.infn.it/~pagano/low_ell_data%20sets/sroll2/

[87] https://github.com/HTJense/pyWMAP
[88] https://github.com/ACTCollaboration/pyactlike
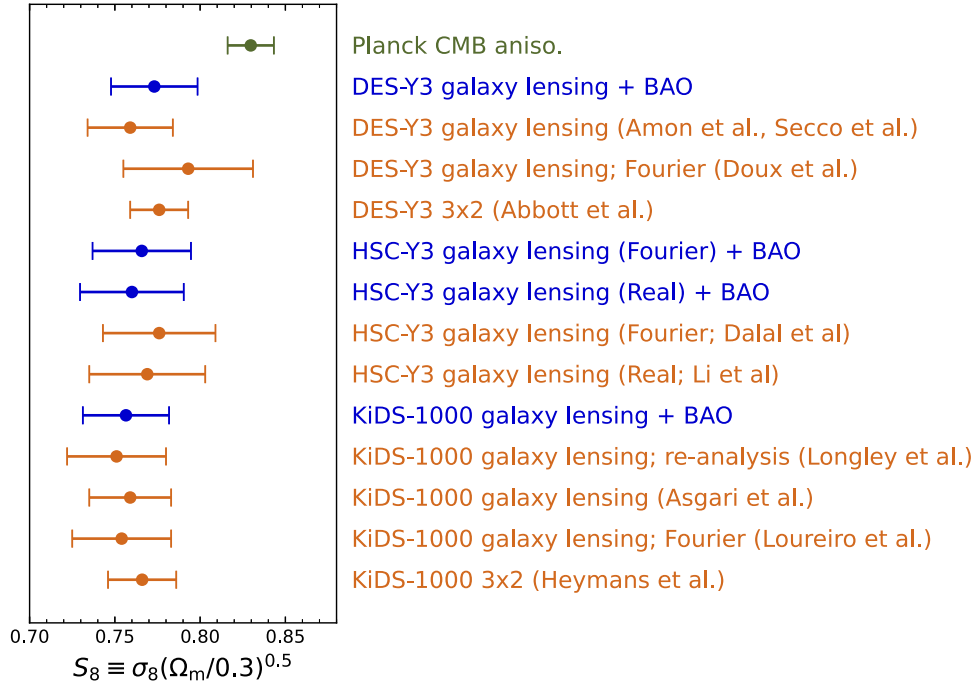[89] https://github.com/mraveri/tensiometer/

Figure 15. Comparison of $\sigma_8(\Omega_m/0.3)^{0.5}$ constraints from a consistent reanalysis of galaxy lensing (blue) with results from the literature (orange).

the galaxy lensing analysis by the KiDS Collaboration (Asgari et al. 2021) and its Fourier variant (Loureiro et al. 2022), and the 3×2 pt analysis by the KiDS Collaboration (Heymans et al. 2021). The HSC-Y3 results are consistent with those from Dalal et al. (2023) and Li et al. (2023). Apart from the differences outlined above (including our choices of priors), it should be noted that some of the constraints reported in the literature do not use the marginalized mean and standard error as we do, but might report quantities such as the multivariate maximum posterior (MAP) and its credible interval calculated using its projected joint highest posterior density (PJ-HPD; e.g., Asgari et al. 2021).

Appendix D
Parameter Dependence of CMB and Galaxy Lensing

CMB lensing constraints on parameters arise from two different ranges of scales. First, on small scales, the CMB lensing power spectrum primarily probes the high-k power-law tail of the matter power spectrum in projection; this implies that CMB lensing parameter constraints can be well approximated by a parameter combination $\sigma_8^\alpha \Omega_m^\beta h^\gamma$, where α, β, γ are constants (Planck Collaboration et al. 2016c; Baxter & Sherwin 2021). On the other hand, much of our CMB lensing power spectrum constraining power also arises from intermediate and large scales, where, due to projection of the matter power spectrum near the peak, the lensing spectrum deviates from this high-L power law, providing a different sensitivity to the matter–radiation equality multipole $L_{eq} \sim (\Omega_m^{0.6} h)$. Therefore, considering the 3D σ_8, Ω_m, h parameter space, the two constraints arising from CMB lensing power spectrum constraints define two surfaces; their intersection implies that the CMB lensing power spectrum constraints define a line in this space. Now we can easily explain why the constraint on σ_8 when combining with BAO (as seen in Figure 16) is so tight:

BAO defines another surface in this space, so that the intersection of the BAO and lensing constraints is a point (or a small region in parameter space; see left panel of Figure 17).

In contrast, galaxy lensing generally does not probe the large-scale regime of scales approaching the matter power spectrum peak; effectively, it only provides one small-scale constraint within the σ_8, Ω_m, h space, defining a single surface. Adding the BAO data, which define a different surface, the intersection gives a line-shaped constraint (instead of a point as for the CMB lensing and BAO combination; see right panel of Figure 17). This explains why the σ_8 constraint is much broader and shows a significant degeneracy with the matter density.
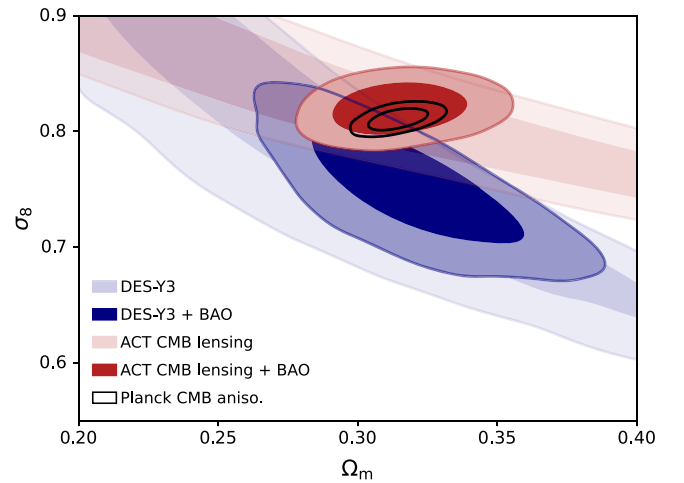

Figure 16. Constraints in the $\sigma_8 - \Omega_m$ plane when combining ACT CMB lensing (red) or DES galaxy lensing (blue) with galaxy BAO. The posteriors in the absence of BAO are shown in lighter shades and are constrained well roughly along the $\sigma_8(\Omega_m/0.3)^{0.25}$ and $\sigma_8(\Omega_m/0.3)^{0.5}$ directions for CMB and galaxy lensing, respectively.
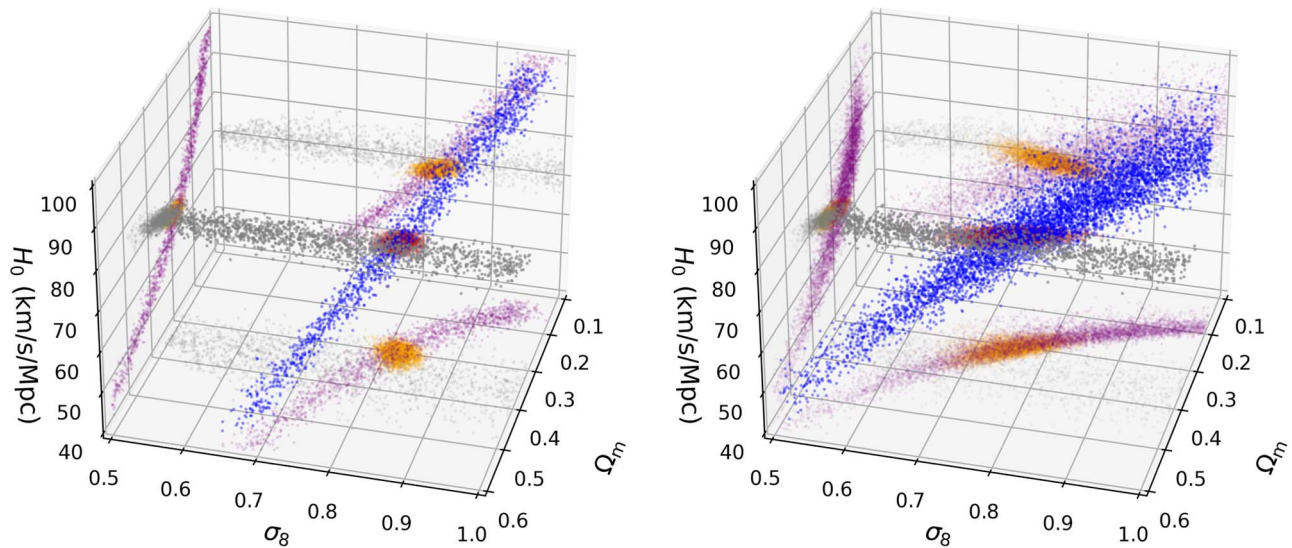
Figure 17. Distribution of MCMC samples for weak lensing in the σ_8–Ω_m–H_0 space. Left: CMB lensing. Galaxy BAO samples are shown in gray; their density does not depend on σ_8. Due to the large range of scales probed by CMB lensing, shown here for ACT DR6 (blue in 3D; purple in projection), they form a line in this space. The intersection of ACT CMB lensing with BAO (red in 3D; orange in projection) provides a tight constraint on σ_8. Right: galaxy lensing. In contrast, the galaxy weak-lensing samples define a surface owing to their not probing the large-scale regime, shown here for DES-Y3 for illustration (blue in 3D; purple in projection). The intersection with BAO (red in 3D; orange in projection) provides weaker constraints on σ_8.

We have verified this explanation with a simple exercise: we perform an analysis on mock CMB lensing data, artificially adjusting the errors to vary the scales from which the information originates, while holding the total signal-to-noise ratio constant. When we shift the mock CMB lensing information only to arise from small scales, $L > 2000$, the shapes of the parameter constraint contours and the constraints on σ_8 show a close resemblance to the constraints from the combination of galaxy weak lensing and BAO.

ORCID iDs

Mathew S. Madhavacheril ⓘ https://orcid.org/0000-0001-6740-5350
Peter Doze ⓘ https://orcid.org/0000-0002-2408-0813
Kirsten R. Hall ⓘ https://orcid.org/0000-0002-4176-845X
Matt Hilton ⓘ https://orcid.org/0000-0002-8490-8117
Kenda Knowles ⓘ https://orcid.org/0000-0002-8452-0825
Kavilan Moodley ⓘ https://orcid.org/0000-0001-6606-7142
Tony Mroczkowski ⓘ https://orcid.org/0000-0003-3816-5372
David N. Spergel ⓘ https://orcid.org/0000-0002-5151-0006
Edward J. Wollack ⓘ https://orcid.org/0000-0002-7567-4451

References

Abazajian, K. N., Adshead, P., Ahmed, Z., et al. 2016, arXiv:1610.02743
Abbott, T. M. C., Aguena, M., Alarcon, A., et al. 2022, PhRvD, 105, 023520
Abe, S., Asami, S., Eizuka, M., et al. 2023, PhRvL, 130, 051801
Ade, P. A. R., Akiba, Y., Anthony, A. E., et al. 2014, PhRvL, 113, 021301
Aiola, S., Calabrese, E., Maurin, L., et al. 2020, JCAP, 2020, 047
Aker, M., Beglarian, A., Behrens, J., et al. 2021, arXiv:2105.08533
Alam, S., Ata, M., Bailey, S., et al. 2017, MNRAS, 470, 2617
Alam, S., Aubert, M., Avila, S., et al. 2021, PhRvD, 103, 083533
Allison, R., Caucal, P., Calabrese, E., Dunkley, J., & Louis, T. 2015, PhRvD, 92, 123535
Alonso, D., Sanchez, J., Slosar, A. & LSST Dark Energy Science Collaboration 2019, MNRAS, 484, 4127
Amon, A., & Efstathiou, G. 2022, MNRAS, 516, 5355
Amon, A., Gruen, D., Troxel, M. A., et al. 2022, PhRvD, 105, 023514
Aricò, G., Angulo, R. E., Zennaro, M., et al. 2023, A&A, 678, A109

Asgari, M., Lin, C.-A., Joachimi, B., et al. 2021, A&A, 645, A104
Ashtari Esfahani, A., Asner, D. M., Böser, S., et al. 2017, JPhG, 44, 054004
Ashtari Esfahani, A., Betancourt, M., Bogorad, Z., et al. 2021, PhRvC, 103, 065501
Astropy Collaboration, Price-Whelan, A. M., Sipőcz, B. M., et al. 2018, AJ, 156, 123
Astropy Collaboration, Robitaille, T. P., Tollerud, E. J., et al. 2013, A&A, 558, A33
Atkins, Z., Duivenvoorden, A. J., Coulton, W. R., et al. 2023, JCAP, 2023, 073
Aylor, K., Joy, M., Knox, L., et al. 2019, ApJ, 874, 4
Battaglia, N., Ferraro, S., Schaan, E., & Spergel, D. N. 2017, JCAP, 2017, 040
Baxter, E. J., Keisler, R., Dodelson, S., et al. 2015, ApJ, 806, 247
Baxter, E. J., Raghunathan, S., Crawford, T. M., et al. 2018, MNRAS, 476, 2674
Baxter, E. J., & Sherwin, B. D. 2021, MNRAS, 501, 1823
Benoit-Lévy, A., Déchelette, T., Benabed, K., et al. 2013, A&A, 555, A37
Beutler, F., Blake, C., Colless, M., et al. 2011, MNRAS, 416, 3017
Bianchini, F., Wu, W. L. K., Ade, P. A. R., et al. 2020, ApJ, 888, 119
BICEP2 Collaboration, Keck Array Collaboration, Ade, P. A. R., et al. 2016, ApJ, 833, 228
Birrer, S., Shajib, A. J., Galan, A., et al. 2020, A&A, 643, A165
Bolliet, B., Colin Hill, J., Ferraro, S., Kusiak, A., & Krolewski, A. 2023, JCAP, 2023, 039
Brieden, S., Gil-Marín, H., & Verde, L. 2023, JCAP, 2023, 023
Brout, D., Scolnic, D., Popovic, B., et al. 2022, ApJ, 938, 110
Calabrese, E., Slosar, A., Melchiorri, A., Smoot, G. F., & Zahn, O. 2008, PhRvD, 77, 123531
Carron, J., Mirmelstein, M., & Lewis, A. 2022, JCAP, 2022, 039
Casarini, L., Bonometto, S. A., Tessarotto, E., & Corasaniti, P. S. 2016, JCAP, 2016, 008
Casarini, L., Macciò, A. V., & Bonometto, S. A. 2009, JCAP, 2009, 014
Chang, C., Omori, Y., Baxter, E. J., et al. 2023, PhRvD, 107, 023530
Chang, C., Pujol, A., Mawdsley, B., et al. 2018, MNRAS, 475, 3165
Choi, S. K., Hasselfield, M., Ho, S.-P. P., et al. 2020, JCAP, 2020, 045
Chung, E., Foreman, S., & van Engelen, A. 2020, PhRvD, 101, 063534
Comparat, J., Delubac, T., Jouvel, S., et al. 2016, A&A, 592, A121
Cooke, R. J., Pettini, M., & Steidel, C. C. 2018, ApJ, 855, 102
Dalal, R., Li, X., Nicola, A., et al. 2023, PhRvD, in press (arXiv:2304.00701)
D'Amico, G., Donath, Y., Lewandowski, M., Senatore, L., & Zhang, P. 2022, arXiv:2206.08327
Darwish, O., Madhavacheril, M. S., Sherwin, B. D., et al. 2021, MNRAS, 500, 2250
Darwish, O., Sherwin, B. D., Sailer, N., Schaan, E., & Ferraro, S. 2022, PhRvD, 107, 043519
Das, S., Sherwin, B. D., Aguirre, P., et al. 2011, PhRvL, 107, 021301

Dawson, K. S., Schlegel, D. J., Ahn, C. P., et al. 2013, AJ, 145, 10
DESI Collaboration, Aghamousa, A., Aguilar, J., et al. 2016, arXiv:1611.00036
Dey, A., Schlegel, D. J., Lang, D., et al. 2019, AJ, 157, 168
Di Valentino, E., Brinckmann, T., Gerbino, M., et al. 2018, JCAP, 2018, 017
Di Valentino, E., Melchiorri, A., & Silk, J. 2020, NatAs, 4, 196
Doux, C., Jain, B., Zeurcher, D., et al. 2022, MNRAS, 515, 1942
du Mas des Bourboux, H., Rich, J., Font-Ribera, A., et al. 2020, ApJ, 901, 153
Dutcher, D., Balkenhol, L., Ade, P. A. R., et al. 2021, PhRvD, 104, 022003
Edge, A., Sutherland, W., Kuijken, K., et al. 2013, Msngr, 154, 32
Efstathiou, G., & Bond, J. R. 1999, MNRAS, 304, 75
Efstathiou, G., & Gratton, S. 2021, OJAp, 4, 8
Eisenstein, D. J., & Hu, W. 1998, ApJ, 496, 605
Eisenstein, D. J., Weinberg, D. H., Agol, E., et al. 2011, AJ, 142, 72
Farren, G. S., Philcox, O. H. E., & Sherwin, B. D. 2022, PhRvD, 105, 063503
Faúndez, M. A., Arnold, K., Baccigalupi, C., et al. 2020, ApJ, 893, 85
Fowler, J., Niemack, M., Dicker, S., et al. 2007, ApOpt, 46, 3444
Freedman, W. L., Madore, B. F., Hatt, D., et al. 2019, ApJ, 882, 34
García-García, C., Ruiz-Zapatero, J., Alonso, D., et al. 2021, JCAP, 2021, 030
Gatti, M., Jain, B., Chang, C., et al. 2022, PhRvD, 106, 083509
Geach, J. E., & Peacock, J. A. 2017, NatAs, 1, 795
Gelman, A., & Rubin, D. B. 1992, StaSc, 7, 457
Górski, K. M., Hivon, E., Banday, A. J., et al. 2005, ApJ, 622, 759
Hamana, T., Shirasaki, M., Miyazaki, S., et al. 2020, PASJ, 72, 16
Hang, Q., Alam, S., Peacock, J. A., & Cai, Y.-C. 2021, MNRAS, 501, 1481
Hanson, D., Challinor, A., Efstathiou, G., & Bielewicz, P. 2011, PhRvD, 83, 043005
He, A., Ivanov, M. M., An, R., & Gluscevic, V. 2023, ApJL, 954, L8
He, S., Alam, S., Ferraro, S., Chen, Y.-C., & Ho, S. 2018, NatAs, 2, 401
Heymans, C., Tröster, T., Asgari, M., et al. 2021, A&A, 646, A140
Hikage, C., Oguri, M., Hamana, T., et al. 2019, PASJ, 71, 43
Hill, J. C., Calabrese, E., Aiola, S., et al. 2022, PhRvD, 105, 123536
Hinshaw, G., Larson, D., Komatsu, E., et al. 2013, ApJS, 208, 19
Hivon, E., Górski, K. M., Netterfield, C. B., et al. 2002, ApJ, 567, 2
Hou, J., Sánchez, A. G., Ross, A. J., et al. 2021, MNRAS, 500, 1201
Hu, W., DeDeo, S., & Vale, C. 2007, NJPh, 9, 441
Hu, W., & Okamoto, T. 2002, ApJ, 574, 566
Hunter, J. D. 2007, CSE, 9, 90
Ivanov, M. M., Philcox, O. H. E., Cabass, G., et al. 2023, PhRvD, 107, 083515
Jeffrey, N., Gatti, M., Chang, C., et al. 2021, MNRAS, 505, 4626
Knox, L., & Millea, M. 2020, PhRvD, 101, 043533
Krolewski, A., Ferraro, S., & White, M. 2021, JCAP, 2021, 028
Leauthaud, A., Saito, S., Hilbert, S., et al. 2017, MNRAS, 467, 3024
Lesgourgues, J., & Pastor, S. 2006, PhR, 429, 307
Lewis, A. 2019, arXiv:1910.13970
Lewis, A., & Challinor, A. 2006, PhR, 429, 1
Lewis, A., Challinor, A., & Lasenby, A. 2000, ApJ, 538, 473
Li, X., Zhang, T., Sugiyama, S., et al. 2023, arXiv:2304.00702
Longley, E. P., Chang, C., Walter, C. W., et al. 2023, MNRAS, 520, 5016
Loureiro, A., Whittaker, L., Spurio Mancini, A., et al. 2022, A&A, 665, A56
MacCrann, N., Sherwin, B. D., Qu, F. J., et al. 2023, ApJ, in press
Madhavacheril, M., Sehgal, N., Allison, R., et al. 2015, PhRvL, 114, 151302
Madhavacheril, M. S., & Hill, J. C. 2018, PhRvD, 98, 023534
Madhavacheril, M. S., Sifón, C., Battaglia, N., et al. 2020, ApJL, 903, L13
Madhavacheril, M. S., Smith, K. M., Sherwin, B. D., & Naess, S. 2021, JCAP, 2021, 028
Mandelbaum, R. 2018, ARA&A, 56, 393
Maniyar, A. S., Ali-Haïmoud, Y., Carron, J., Lewis, A., & Madhavacheril, M. S. 2021, PhRvD, 103, 083524
Martini, P., Bailey, S., Besuner, R. W., et al. 2018, Proc. SPIE, 10702, 107021F
McCarthy, F., Foreman, S., & van Engelen, A. 2021, PhRvD, 103, 103538
McCarthy, F., Hill, J. C., & Madhavacheril, M. S. 2022, PhRvD, 105, 023517
McCarthy, F., Madhavacheril, M. S., & Maniyar, A. S. 2023, PhRvD, 108, 083522
Mead, A. J., Brieden, S., Tröster, T., & Heymans, C. 2021, MNRAS, 502, 1401
Mead, A. J., Heymans, C., Lombriser, L., et al. 2016, MNRAS, 459, 1468
Mead, A. J., Peacock, J. A., Heymans, C., Joudaki, S., & Heavens, A. F. 2015, MNRAS, 454, 1958

Millea, M., Daley, C. M., Chou, T. L., et al. 2021, ApJ, 922, 259
Mirmelstein, M., Carron, J., & Lewis, A. 2019, PhRvD, 100, 123509
Monreal, B., & Formaggio, J. A. 2009, PhRvD, 80, 051301
Morris, T. W., Bustos, R., Calabrese, E., et al. 2022, PhRvD, 105, 042004
Mossa, V., Stöckel, K., Cavanna, F., et al. 2020, Natur, 587, 210
Namikawa, T., Hanson, D., & Takahashi, R. 2013, MNRAS, 431, 609
Nguyen, N.-M., Huterer, D., & Wen, Y. 2023, PhRvL, 131, 111001
Okamoto, T., & Hu, W. 2003, PhRvD, 67, 083002
Osborne, S. J., Hanson, D., & Doré, O. 2014, JCAP, 2014, 024
Pagano, L., Delouis, J. M., Mottet, S., Puget, J. L., & Vibert, L. 2020, A&A, 635, A99
Pan, Z., & Knox, L. 2015, MNRAS, 454, 3200
Peebles, P. J. E., & Ratra, B. 1988, ApJL, 325, L17
Peloton, J., Schmittfull, M., Lewis, A., Carron, J., & Zahn, O. 2017, PhRvD, 95, 043508
Philcox, O. H. E., Farren, G. S., Sherwin, B. D., Baxter, E. J., & Brout, D. J. 2022, PhRvD, 106, 063530
Philcox, O. H. E., & Ivanov, M. M. 2022, PhRvD, 105, 043517
Planck Collaboration, Adam, R., Ade, P. A. R., et al. 2016a, A&A, 594, A10
Planck Collaboration, Ade, P. A. R., Aghanim, N., et al. 2014, A&A, 571, A17
Planck Collaboration, Ade, P. A. R., Aghanim, N., et al. 2016b, A&A, 594, A13
Planck Collaboration, Ade, P. A. R., Aghanim, N., et al. 2016c, A&A, 594, A15
Planck Collaboration, Ade, P. A. R., Aghanim, N., et al. 2016d, A&A, 594, A24
Planck Collaboration, Aghanim, N., Akrami, Y., et al. 2020a, A&A, 641, A1
Planck Collaboration, Aghanim, N., Akrami, Y., et al. 2020b, A&A, 641, A5
Planck Collaboration, Aghanim, N., Akrami, Y., et al. 2020c, A&A, 641, A6
Planck Collaboration, Aghanim, N., Akrami, Y., et al. 2020d, A&A, 641, A8
Planck Collaboration, Akrami, Y., Andersen, K. J., et al. 2020e, A&A, 643, A42
Pogosian, L., Raveri, M., Koyama, K., et al. 2022, NatAs, 6, 1484
Qu, F., Sherwin, B., Madhavacheril, M., et al. 2024, ApJ, 962, 112
Qu, F. J., Challinor, A., & Sherwin, B. D. 2023, PhRvD, 108, 063518
Raghunathan, S., Bianchini, F., & Reichardt, C. L. 2018, PhRvD, 98, 043506
Raghunathan, S., Nadathur, S., Sherwin, B. D., & Whitehorn, N. 2020, ApJ, 890, 168
Raghunathan, S., Patil, S., Baxter, E., et al. 2019, PhRvL, 123, 181301
Raveri, M., & Doux, C. 2021, PhRvD, 104, 043504
Raveri, M., Zacharegkas, G., & Hu, W. 2020, PhRvD, 101, 103527
Riess, A. G., Yuan, W., Macri, L. M., et al. 2022, ApJL, 934, L7
Rogers, K. K., Hložek, R., Laguë, A., et al. 2023, JCAP, 2023, 023
Rosenberg, E., Gratton, S., & Efstathiou, G. 2022, MNRAS, 517, 4620
Ross, A. J., Samushia, L., Howlett, C., et al. 2015, MNRAS, 449, 835
Sailer, N., Schaan, E., & Ferraro, S. 2020, PhRvD, 102, 063517
Schaan, E., & Ferraro, S. 2019, PhRvL, 122, 181301
Schmittfull, M., & Seljak, U. 2018, PhRvD, 97, 123540
Schmittfull, M. M., Challinor, A., Hanson, D., & Lewis, A. 2013, PhRvD, 88, 063012
Secco, L. F., Samuroff, S., Krause, E., et al. 2022, PhRvD, 105, 023515
Sherwin, B. D., Dunkley, J., Das, S., et al. 2011, PhRvL, 107, 021302
Sherwin, B. D., van Engelen, A., Sehgal, N., et al. 2017, PhRvD, 95, 123529
Smith, K. M., Zahn, O., & Doré, O. 2007, PhRvD, 76, 043510
Smith, T. L., Poulin, V., & Simon, T. 2023, PhRvD, 108, 103525
SO Collaboration 2019, JCAP, 2019, 056
Spergel, D. N., Verde, L., Peiris, H. V., et al. 2003, ApJS, 148, 175
Stein, G., Alvarez, M. A., Bond, J. R., van Engelen, A., & Battaglia, N. 2020, JCAP, 2020, 012
Stompor, R., & Efstathiou, G. 1999, MNRAS, 302, 735
Strauss, M. A., Weinberg, D. H., Lupton, R. H., et al. 2002, AJ, 124, 1810
Surrao, K. M., Philcox, O. H. E., & Hill, J. C. 2023, PhRvD, 107, 083521
Thornton, R., Ade, P., Aiola, S., et al. 2016, ApJS, 227, 21
Torrado, J., & Lewis, A. 2021, JCAP, 2021, 057
van Engelen, A., Keisler, R., Zahn, O., et al. 2012, ApJ, 756, 142
White, M., Zhou, R., DeRose, J., et al. 2022, JCAP, 2022, 007
Yu, B., Seljak, U., Li, Y., & Singh, S. 2023, JCAP, 2023, 057
Zaldarriaga, M. 1997, PhRvD, 55, 1822
Zonca, A., Singer, L., Lenz, D., et al. 2019, JOSS, 4, 1298
Zuntz, J., Paterno, M., Jennings, E., et al. 2015, A&C, 12, 45